MOLECULAR BIOLOGY

Tumor suppressor FRMD3 controls mammary epithelial cell fate determination via notch signaling pathway

Ji Ma[1]†, Yuqing Gong[1]†, Xiaoran Sun[1,2]†, Cheng Liu[1], Xueying Li[1], Yi Sun[1], Decao Yang[1], Junming He[1], Mengyuan Wang[1], Juan Du[1], Jing Zhang[1], Weizhi Xu[1], Tianzhuo Wang[1], Xiaochun Chi[1], Yan Tang[1], Jiagui Song[1], Yunling Wang[3], Fei Ma[4]*, Ceshi Chen[5]*, Hongquan Zhang[1]*, Jun Zhan[1]*

The luminal-to-basal transition in mammary epithelial cells (MECs) is accompanied by changes in epithelial cell lineage plasticity; however, the underlying mechanism remains elusive. Here, we report that deficiency of *Frmd3* inhibits mammary gland lineage development and induces stemness of MECs, subsequently leading to the occurrence of triple-negative breast cancer. Loss of *Frmd3* in *PyMT* mice results in a luminal-to-basal transition phenotype. Single-cell RNA sequencing of MECs indicated that knockout of *Frmd3* inhibits the Notch signaling pathway. Mechanistically, FERM domain-containing protein 3 (FRMD3) promotes the degradation of Disheveled-2 by disrupting its interaction with deubiquitinase USP9x. FRMD3 also interrupts the interaction of Disheveled-2 with CK1, FOXK1/2, and NICD and decreases Disheveled-2 phosphorylation and nuclear localization, thereby impairing Notch-dependent luminal epithelial lineage plasticity in MECs. A low level of FRMD3 predicts poor outcomes for breast cancer patients. Together, we demonstrated that FRMD3 is a tumor suppressor that functions as an endogenous activator of the Notch signaling pathway, facilitating the basal-to-luminal transformation in MECs.

INTRODUCTION

Triple-negative breast cancer (TNBC) constitutes approximately 15 to 20% of breast cancers and is an aggressive subtype with a poor overall prognosis characterized by a lack of expression of estrogen receptor (ER), progesterone receptor (PR), and human epidermal growth factor receptor 2 (HER2) (*1*). The basal-like subtype of TNBC is the most common and is characterized by a high proliferation rate, basal epithelial markers, and low expression of luminal genes (*2*, *3*). Claudin-low tumors are characterized by low to absent expression of luminal differentiation markers with marked enrichment of epithelial-to-mesenchymal (EMT) transition markers and cancer stem cell (CSC)–like features. TNBC is the most difficult subtype of breast cancer to treat because of its aggressive clinical behavior and lack of therapeutic targets (*4*).

CSCs, also known as tumor-initiating cells, a subpopulation with high tumor initiation and repopulation abilities, have extensive self-renewal potential, enabling them to recreate the heterogeneity of the original tumor by asymmetric division (*5*). Breast CSCs (bCSCs) can arise from transformed normal stem cells via the acquisition of genetic mutations; normal non-stem epithelial cells in which self-renewal is acquired by oncogenic events and transformation; or differentiated

cancer cells that dedifferentiate into a CSC-like phenotype, as a paradigm of cellular plasticity (*6*, *7*). Human breast carcinomas are heterogeneous; unlike other common epithelial cancers, breast tumors have complicated pathological and molecular features. Gene expression profiling of epithelial tumors has identified distinct subtypes with differences in survival and response to therapy. Breast cancer is classified into luminal A, luminal B, HER2-enriched, basal-like, and claudin-low subtypes (*8*). This classification based on gene expression patterns speculates on the origin of breast cancer and determines subtypes of tumors, which may represent the transformation of stem cells, stagnation at particular developmental stages, or direct transformation of mature cell types (*8*).

The mammary gland (MG) is used to investigate the regulation of stem cells that undergo morphogenesis after birth and their development reflects the different physiological stages. The MG epithelium is hierarchically organized and composed of highly elongated basal cells with contractile capacity and luminal cells that produce milk (*9*, *10*). Mammary stem cells (MaSCs) are important for organ development and maintaining tissue homeostasis; MaSCs are at the top of the hierarchy and give rise to mature epithelium of luminal or myoepithelial lineage via a series of lineage-restricted intermediates (*11*).

The mechanisms and pathways that regulate the self-renewal and differentiation of MaSCs have prophylactic and therapeutic potential for breast cancer. A variety of signaling pathways and modulators have been found involved in the regulation of mammary epithelial hierarchy, largely through the characterization of mammary epithelial subsets in mice. Given the similarities between normal stem cells and CSCs, it is expected that a number of key developmental pathways are implicated in the regulation of normal and malignant stem cells. For example, the Notch signaling pathway, Wnt/β-catenin pathway, and Hedgehog pathway were found to regulate MaSC fate decision (*5*, *12*). Several key transcription factors control the differentiation hierarchy of the MG (*7*, *13*); e.g., Slug and Sox9 are key determinants of the MaSC state. In addition, it was also found that up-regulation of ZEB1

[1]Program for Cancer and Cell Biology, Department of Human Anatomy, Histology, and Embryology, School of Basic Medical Sciences, and Peking University International Cancer Institute, State Key Laboratory of Molecular Oncology, Peking University Health Science Center, Beijing 100191, China. [2]Department of Pathology, Peking University Health Science Center, Beijing 100191, China. [3]Institute of Cardiovascular Research, Peking University Health Science Center, Beijing 100191, China. [4]National Cancer Center, State Key Laboratory of Molecular Oncology, Cancer Hospital, Chinese Academy of Medical Sciences and Peking Union Medical College, Beijing, China. [5]Key Laboratory of Animal Models and Human Disease Mechanisms of the Chinese Academy of Sciences and Yunnan Province, Kunming Institute of Zoology, Chinese Academy of Sciences, Kunming, Yunnan 650223, China.
*Corresponding author. Email: zhanjun@bjmu.edu.cn (J.Z.); hongquan.zhang@bjmu.edu.cn (H.Z.); chenc@mail.kiz.ac.cn (C.C.); drmafei@126.com (F.M.)
†These authors contributed equally to this work.

induces non-CSCs to CSCs and Gata-3 is a crucial regulator of the luminal lineages (*14*, *15*).

The Notch signaling pathway plays a crucial role in maintaining the differentiation status of unipotent luminal epithelial progenitor cells in MG development. Activation of the Notch signaling pathway induces differentiation of MaSCs toward luminal epithelial progenitor cells, drives basal cells to acquire the characteristics of ER-negative luminal cells, and promotes the gradual movement of transformed cells to the duct lumen (*16*). Depletion of the *Fermt2* (encoding gene of kindlin-2) promotes the activation of the Notch signaling pathway, impairs the differentiation of mouse acinar epithelium, and leads to epithelial cells remaining in the state of unipotent progenitor cells on the lumen (*17*). In contrast, inhibition of Notch signaling by knocking down/disrupting *Cbf-1* can induce transdifferentiation from luminal to basal by up-regulating ectopic proliferation of MaSC (*18*). Conversely, knockout of *Numb/Numbl* (encoding a Notch signaling inhibitor) leads to the down-regulation of basal layer–specific genes and up-regulation of luminal layer–specific genes in breast epithelium (*19*). Thus, maintaining the luminal progenitor status by the Notch signaling pathway lays down the basis for elucidating the molecular mechanism of FRMD3 deficiency-inducing mammary epithelial cell (MEC) stemness.

FERM domain-containing protein 3 (FRMD3) is a member of the protein 4.1 superfamily; members of this superfamily contain a highly conserved membrane-association domain, FERM. FRMD3 is a single-pass membrane protein primarily found in ovaries; in erythrocytes, a similar protein determines the shape of red blood cells, but the function of the encoded protein has not been determined. FERM family protein Merlin/NF2 was known to regulate stem/progenitor cell differentiation and tumorigenesis in the liver (*20*, *21*). FRMD3 is a putative tumor suppressor gene and may play an important in the development of cancer (*22*). Here, we report that FRMD3 promotes the maintenance of the MECs hierarchy and may regulate MaSC/bCSC fate determination.

RESULTS

Decreased FRMD3 is predictive of poor outcome in patients with breast cancer

By analyzing The Cancer Genome Atlas (TCGA) human breast cancer dataset (https://xenabrowser.net/heatmap/), we found that *FRMD3* was expressed at a significantly lower level in breast cancer tissues compared with normal breast tissues (Fig. 1A) and a reduced level of *FRMD3* was correlated with increased malignancy of breast cancer (Fig. 1B). According to the DNA methylation database, the promotor methylation level of *FRMD3* is significantly higher in breast cancer compared with normal breast tissues (Fig. 1C). To confirm the down-regulation of FRMD3 in breast cancer, we performed immunohistochemistry (IHC) analyses using human breast cancer tissue microarrays. Compared with the normal breast epithelium, FRMD3 expression was lower in breast cancer and was further decreased in more malignant TNBC (Fig. 1D and table S1). Kaplan-Meier analysis showed that low FRMD3 expression was strongly associated with a poor prognosis (Fig. 1, E and F). Furthermore, we detected high methylation of the *FRMD3* promoter in MDA-MB-231 TNBC cells (Fig. 1, G and H), which have low expression of FRMD3. The methyltransferase inhibitor 5-AZA-dC partially restored the expression of FRMD3 in MCF-7 and MDA-MB-231 cells (Fig. 1, I and J). These results indicated that low FRMD3 expression is a risk factor for breast cancer.

Deficiency of *Frmd3* impairs luminal epithelium development and induces TNBC-like tumors in mice

Given that FRMD3 expression is low in breast cancer, could its depletion induce breast tumorigenesis? We thus generated *Frmd3*$^{-/-}$ mice (fig. S1A) and followed them for 18 months. The mice began to develop mammary tumors at the age of 8 months, with a total tumor incidence of 65% (Fig. 2A). The tumors had abundant blood vessels and adhere to surrounding tissues (fig. S1B). Gene expression profiling has led to the classification of mammary tumors into five molecular subtypes (*23*) luminal A, luminal B, HER2-positive, claudin-low, and basal-like (*24*–*26*). Comparison of gene expression profiles could identify the breast cancer subtype and may suggest the cell of origin of the tumor (*27*). Therefore, we evaluated the characteristics of these tumors. Hematoxylin and eosin staining showed a typical invasive ductal carcinoma morphology (Fig. 2B). Histological and immunostaining analyses revealed two types of *Frmd3*$^{-/-}$ mutant tumors. The majority (~70%) showed glandular differentiation with mild inflammation (type 1) and ~25% were grade 3 carcinomas with syncytial growth, pushing border, large pleomorphic nuclei, conspicuous mitoses, and regions of necrosis (type 2) (Fig. 2B). There were also a few of poorly differentiated or metaplastic carcinomas. All the tumors exhibited heterogeneous regions with squamous (fig. S1C), papillary (fig. S1D), giant cell (fig. S1E), and glandular (fig. S1F) histological characteristics (*28*, *29*). All the tumors were triple-negative (ER$^-$, PR$^-$, and HER2$^-$) (Fig. 2B) and highly proliferative (fig. S1G). In the majority of these tumors (type 1), we observed epithelial tumor cells expressing keratin markers including casein kinase 14 (CK14), CK8, CK5, and α–smooth muscle actin (α-SMA). The expression of these keratin markers was very low in type 2 tumors (Fig. 2C and fig. S1H). Consistently, staining for claudin-3, the epithelial marker E-cadherin, and the mesenchymal marker vimentin showed that type 2 tumors had lost their epithelial identity to a greater degree than type 1 tumors (fig. S1, I to K). Overall, type 1 tumors had lost luminal features and showed TNBC phenotype. The immunostaining characteristics of type 2 tumor cells are most similar to the claudin-low subtype (*26*, *30*, *31*).

We also detected paracancerous tissues. All the premalignant lesions contained MECs with a luminal-to-basal change compared with the wild-type (WT) MECs and decreased the expression of the luminal markers ERα (Fig. 2D), PR (Fig. 2E), and CK8 (Fig. 2F) and increased the expression of the basal marker CK5 (Fig. 2G and fig. S1L). Furthermore, proliferation marker Ki67 was increased in premalignant lesions in *Frmd3*$^{-/-}$ mice (fig. S1M). In summary, *Frmd3* knockout in mammary tissues induces loss of luminal identity and gain of basal properties.

Frmd3 is required to maintain MG development in mice

The epithelium of MG is composed of two main cellular lineages: luminal cells surrounding a central lumen and highly elongated myoepithelial cells in a basal position adjacent to the basement membrane (*11*). The mammary epithelium originating at the nipple is quiescent from birth to puberty. During puberty (at week 3), the ductal epithelium of the mammary anlage invades the mammary fat pad in a process referred to as branching morphogenesis. Until weeks 5 to 6, under the control of hormones and other factors, MECs are highly proliferative, especially for the luminal population that expands fast over the basal population, leading to the enrichment of ER$^+$PR$^+$ luminal cells (*32*). To investigate the function of *Frmd3* in MG development, we analyzed the *Frmd3* mRNA
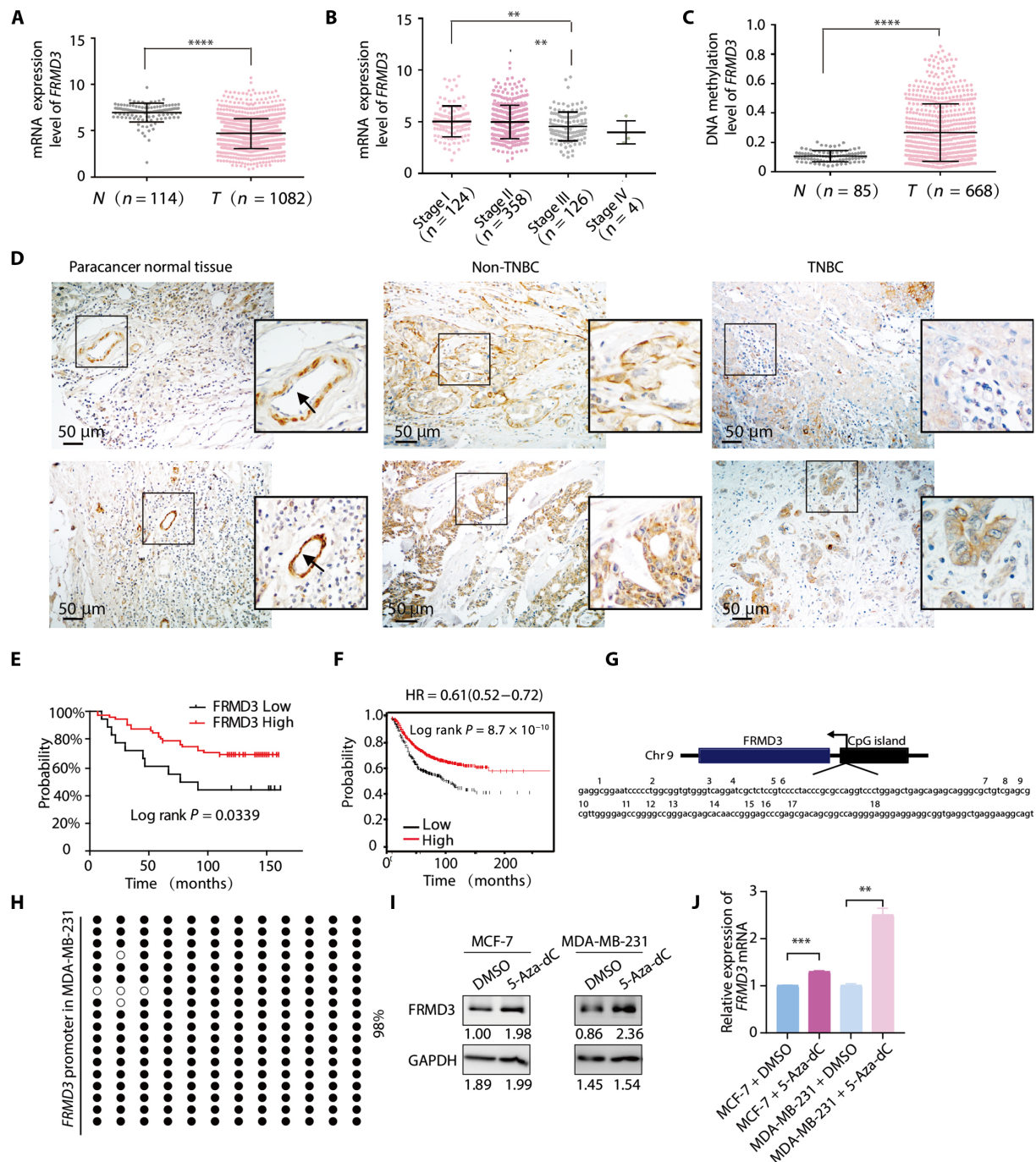
Fig. 1. Decreased FRMD3 is predictive of poor outcomes in patients with breast cancer. (**A** to **C**) Analysis of the TCGA human breast cancer dataset (https://xenabrowser.net/heatmap/). (A) Mean mRNA levels of *FRMD3* in normal breast tissues ($n = 114$) and invasion ductal carcinomas ($n = 1082$). (B) Associations between *FRMD3* mRNA level and TNM stage (converted stage nature 2012) (stage I $n = 124$, stage II $n = 358$, stage III $n = 126$, and stage VI $n = 4$). (C) Mean DNA methylation level of *FRMD3* in normal breast tissues ($n = 85$) and invasion ductal carcinomas ($n = 668$). (**D**) Breast cancer tissue microarray was immunostained using an anti-FRMD3 antibody. Arrows: normal MG. Scale bars, 50 μm. (**E**) Decreased FRMD3 expression correlates with poor overall survival in patients with breast cancer as determined by Kaplan-Meier (KM) analysis ($P < 0.05$, log-rank). (**F**) Using a publicly available database (KM plotter; www.kmplot.com), relapse-free survival curves were analyzed in breast cancer mRNA gene chip. A total of 2032 patients; affy ID: 229893_at; Survival:RFS, split patients by lower quartile; cutoff value used in analysis:112, $P = 8.7 \times 10^{-10}$; log-rank P values were calculated in KM plot database. HR, hazard ratio. (**G**) Schematic diagrams of the fragments for bisulfite sequencing in the CpG islands of *FRMD3*. (**H**) Bisulfite sequencing analyses of DNA methylation in the *FRMD3* promoters were performed in MDA-MB-231 cells. Methylated CG (filled circles) and unmethylated CG (open circles) are represented. The methylation rate (as a percentage) is shown under the panel. Twelve separate subclones were sequenced. (**I** and **J**) MCF-7 and MDA-MB-231 cells were treated with 5-Aza-dC (10 μM), respectively, for 48 hours. The protein expression of FRMD3 was examined by Western blotting (WB) (I). *FRMD3* mRNA levels were examined by quantitative polymerase chain reaction (qPCR) (J) and *GAPDH* was used as an internal reference. Data are shown as means ± SD; **$P < 0.01$, ***$P < 0.001$, and ****$P < 0.0001$, by unpaired Student's t test [(A) to (C), (I), and (J)]. GAPDH, glyceraldehyde-3-phosphate dehydrogenase; DMSO, dimethyl sulfoxide.
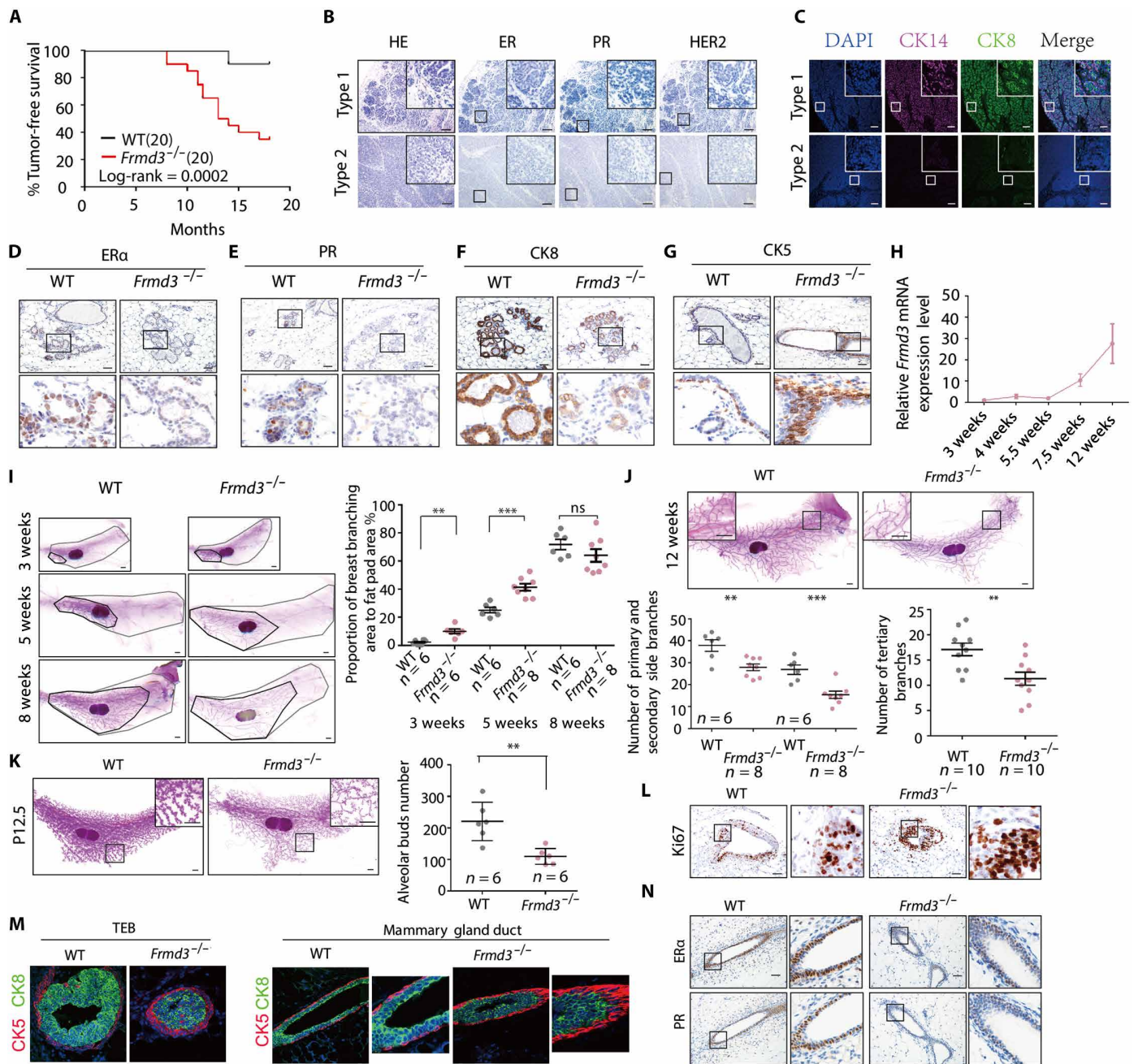
Fig. 2. Depletion of *Frmd3* induced TNBC and impaired luminal epithelium development in mice. (**A**) Kaplan-Meier mammary tumor latency survival curve for WT and *Frmd3*⁻/⁻ mice. (**B**) Hematoxylin and eosin (H&E) and immunohistochemistry (IHC) staining for ERα, PR, and HER2 in two types of *Frmd3*⁻/⁻ mammary tumors. Scale bars, 100 μm. (**C**) Immunofluorescence (IF) staining for basal (Ck14) and luminal (Ck8) markers in two types of Frmd3⁻/⁻ mammary tumors. Scale bars, 100 μm. (**D** to **G**) Representative immunostaining sections for ERα, PR, CK5, and CK8 markers on premalignant MG from wild-type (WT) and *Frmd3*⁻/⁻ female mice. Scale bars, 50 μm. (**H**) RT-qPCR for *FRMD3* in WT MG at the indicated time. (*n* = 3 per group). (**I**) Whole-mount staining of 3-, 5-, and 8-week-old *Frmd3*⁻/⁻ MG and WT littermates. Scale bars, 1 mm. Percent of the mammary ductal area in the whole fat pad is analyzed (six or eight mice per group). (**J**) Whole-mount staining of 12-week-old *Frmd3*⁻/⁻ MG and WT littermates. Scale bars, 1 mm. The numbers of mammary primary and secondary side branches and tertiary branches in the indicated groups were analyzed (6 to 10 mice per group as indicated). (**K**) Whole-mount staining of P12.5 *Frmd3*⁻/⁻ MG and WT littermates. Scale bars, 1 mm. The numbers of mammary alveolar buds in the indicated groups were analyzed (six mice per group). (**L**) IHC for Ki67 in terminal end bud (TEB) of WT and *Frmd3*⁻/⁻ MG at 5 weeks of age. Scale bars, 50 μm. (**M**) Co-IF for Ck5 and Ck8 in TEB of WT and *Frmd3*⁻/⁻ at 5 weeks of age and MG ducts at 8 weeks of age. (**N**) IHC for Era and PR of WT and *Frmd3*⁻/⁻ MG at 8 weeks of age. Scale bars, 50 μm. Data are shown as means ± SD; **P < 0.01, and ***P < 0.001, nonsignificant (ns) by unpaired Student's *t* test [(I) to (K)].

level at a variety of MG developmental stages. Starting from puberty (week 3), *Frmd3* mRNA expression increased gradually to a marked peak at week 7.5 (Fig. 2H).

Next, whole-mount staining was performed to assess the role of Frmd3 in MG organogenesis during puberty. In early puberty (weeks 3 to 5), the MG distribution area of *Frmd3*$^{-/-}$ mice increased. Until late puberty (week 8), the MG distribution area was equal to that of WT littermates (Fig. 2I). Notably, depletion of *Frmd3* resulted in impaired ductal complexity and a decreased number of primary and secondary mammary side branches (Fig. 2J). By week 12, the MG of WT mice had an elaborate network of tertiary branches. By contrast, part of the *Frmd3*$^{-/-}$ MG had virtually no tertiary branches (Fig. 2J). As expected, acinar formation during pregnancy decreased significantly in MG of *Frmd3*$^{-/-}$ compared with WT mice (Fig. 2K).

Terminal end buds (TEBs) promote ductal branching and elongation into the mammary fat pad in puberty. TEBs consist of an outer layer of basal epithelial cap cells and multiple inner layers of luminal epithelial cells. As the most proliferative structure in the pubertal gland, we detected Ki67 expression in TEBs at week 5. *Frmd3*$^{-/-}$ MGs showed increased cell proliferation especially in the cap later (Fig. 2L), underlying a transient fast-growing period in the early puberty. We subjected TEBs to IHC using CK8 (for luminal cell staining) and CK5 (for basal cell staining) antibodies separately. As expected, *Frmd3*$^{-/-}$ glands showed a decreased number of CK8$^+$ luminal cells and an increased number of CK5$^+$ basal cells in TEBs (Fig. 2M). In addition, sections of 8-week-old MG branches in *Frmd3*$^{-/-}$ mice showed increased CK5 and no CK8 expression, compared to the control group (Fig. 2M and fig. S2A). Furthermore, we found that the ER and PR levels decreased in *Frmd3*$^{-/-}$ compared with WT MG (Fig. 2N). Together, these data suggested that *Frmd3* knockout leads to mammary dysplasia by promoting the expansion of basal cells and inhibiting the differentiation of luminal cells.

Deficiency of *Frmd3* leads to the expansion of MaSCs and impairs luminal-lineage determination in MG

To explore the changes in gene transcription caused by the depletion of *Frmd3*, we sorted Lin$^-$ MECs from matched *Frmd3*$^{-/-}$ females and WT littermate control females (8 weeks old) and subjected them to microarray expression profiling. We conducted a gene set enrichment analysis to identify lineage changes in *Frmd3*$^{-/-}$ MECs. Compared with the control group, *Frmd3*$^{-/-}$ MECs exhibited the up-regulation of MaSC (basal MEC) according to MaSC signatures reported by others (*33*, *34*) Furthermore, EMT/CSC-related gene signatures (*35*) were enriched in *Frmd3*$^{-/-}$ MECs (Fig. 3A), suggesting that loss of Frmd3 induces a global luminal-to-basal cell fate change. Compared to the control group, *Frmd3*$^{-/-}$ MECs displayed altered expression of several Gene Ontology groups, including branch elongation of MG duct, epithelial cell differentiation, and positive regulation of G1/S transition of the mitotic cell cycle, which was in the top rank of biological process (fig. S3A). Frmd3 deficiency alters the fate of MECs by influencing the expression of a set of genes.

We next profiled the population using CD24, CD29/CD49f (for luminal and basal MEC subsets), and SCA1 [to distinguish ER$^+$ (Lin$^-$CD29^{lo}SCA1$^+$) and ER$^-$ (Lin$^-$CD29^{lo}SCA1$^-$) luminal subsets] (*32*, *36*). Consistent with the microarray data, fluorescence-activated cell sorting (FACS) analysis revealed an increased MaSC (Lin$^-$CD24$^+$CD29^{hi}) basal/myoepithelial population and a decreased luminal (Lin$^-$CD24^{hi}CD29^{lo}) population in early puberty MGs of *Frmd3*$^{-/-}$ mice compared to WT mice (Fig. 3B). Furthermore,

increased number (Fig. 3, C and D) and large size (Fig. 3E) of mammospheres were observed in *Frmd3*$^{-/-}$ MECs, indicating that Frmd3 deficiency enhances the self-renewal ability of MaSCs.

We next performed clonal expansion assays to assess the ability of single cells to form functional ductal-alveolar structures in Matrigel. Two multicellular structures—small acinus-like structures of luminal epithelial origin and solid spherical colonies of myoepithelial origin—have been reported (*37–39*). In a clonal expansion assay in vitro, loss of *Frmd3* resulted in the formation of more solid spherical colonies and fewer acinus-like structures (Fig. 3, F and G). Assessment of lineage-specific differentiation by immunostaining revealed that organoids from *Frmd3*$^{-/-}$ MECs had stronger CK5 and weaker CK8 expressions (Fig. 3H).

In transplantation assays (*40*), the frequency of mammary repopulating unit is similar in *Frmd3* knockout and WT cells (Fig. 3I), indicating that the repopulating activity of MaSCs derived from Frmd3-deficient glands is similar to those derived from WT glands. This is likely because *Frmd3*$^{-/-}$ MaSCs have higher self-renewal but lower differentiation ability in vivo. Moreover, *Frmd3*$^{-/-}$ mice showed a smaller luminal population at week 5, which expanded and surpassed that of WT mice at week 10 (fig. S3B). Therefore, *Frmd3* depletion promotes the proliferation of MaSCs and restricts their differentiation.

Loss of *Frmd3* increases CSC stemness in *PyMT* tumors

We explored the function of *Frmd3* in the *MMTV-PyMT* mouse model, which develops tumors that exhibit luminal progenitor gene signature profiles and resemble the luminal subtype of human breast cancer (*41*). We crossed the *Frmd3*$^{-/-}$ mice with *MMTV-PyMT* mice and obtained *PyMT/Frmd3*$^{-/-}$ mice. Although the overall tumor-free survival duration of *PyMT/Frmd3*$^{-/-}$ mice was similar to *PyMT* control mice (Fig. 4A), the volume and number of tumors that emerged in *PyMT/Frmd3*$^{-/-}$ mice were markedly larger and more compared with those in *PyMT* control mice at days 120 (Fig. 4, B and C). *PyMT/Frmd3*$^{-/-}$ tumors displayed syncytial growth, a pushing border, and conspicuous areas of necrosis with strong staining of Ki67 at the invasive edge. By contrast, *PyMT* tumors showed glandular differentiation and moderated proliferation (Fig. 4D). Following tumor progression, *PyMT* tumors showed loss of ER and PR expressions and increased HER2 expression. In the late stage of *PyMT* carcinoma, ER$^-$ cells account for >90% of the tumor volume with scattered clusters of ER$^+$ cells in a small area in 80% of *PyMT* mice. In the other 20% of *PyMT* mice, the amount of ER$^+$ cells in tumors was approximately 40 to 50%, suggesting that these tumor cells had not progressed to the most malignant stage (stage 3). *PyMT/Frmd3*$^{-/-}$ tumors at the same stage were ER$^-$ PR$^-$, consistent with the spontaneous tumor phenotype (Fig. 4E). Moreover, the up-regulation of CK5 and down-regulation of CK8 in *PyMT/Frmd3*$^{-/-}$ tumors (Fig. 4F) suggested that Frmd3 deficiency causes loss of luminal markers and promotes transformation of the tumor state.

We next evaluated the function of Frmd3 in breast cancer CSCs. We dissociated primary tumors from *PyMT* and *PyMT/Frmd3*$^{-/-}$ mice and performed mammosphere formation assays in vitro (*42*). Compared with *PyMT* tumor cells, *PyMT/Frmd3*$^{-/-}$ tumor cells formed more and larger mammospheres at day 5 (Fig. 4, G and H). Furthermore, following orthotopic transplantation into 3-week-old WT recipient mice, *PyMT/Frmd3*$^{-/-}$ cells showed a higher tumor incidence (Fig. 4I). Also, *PyMT/Frmd3*$^{-/-}$ tumors contained more tumor-repopulating
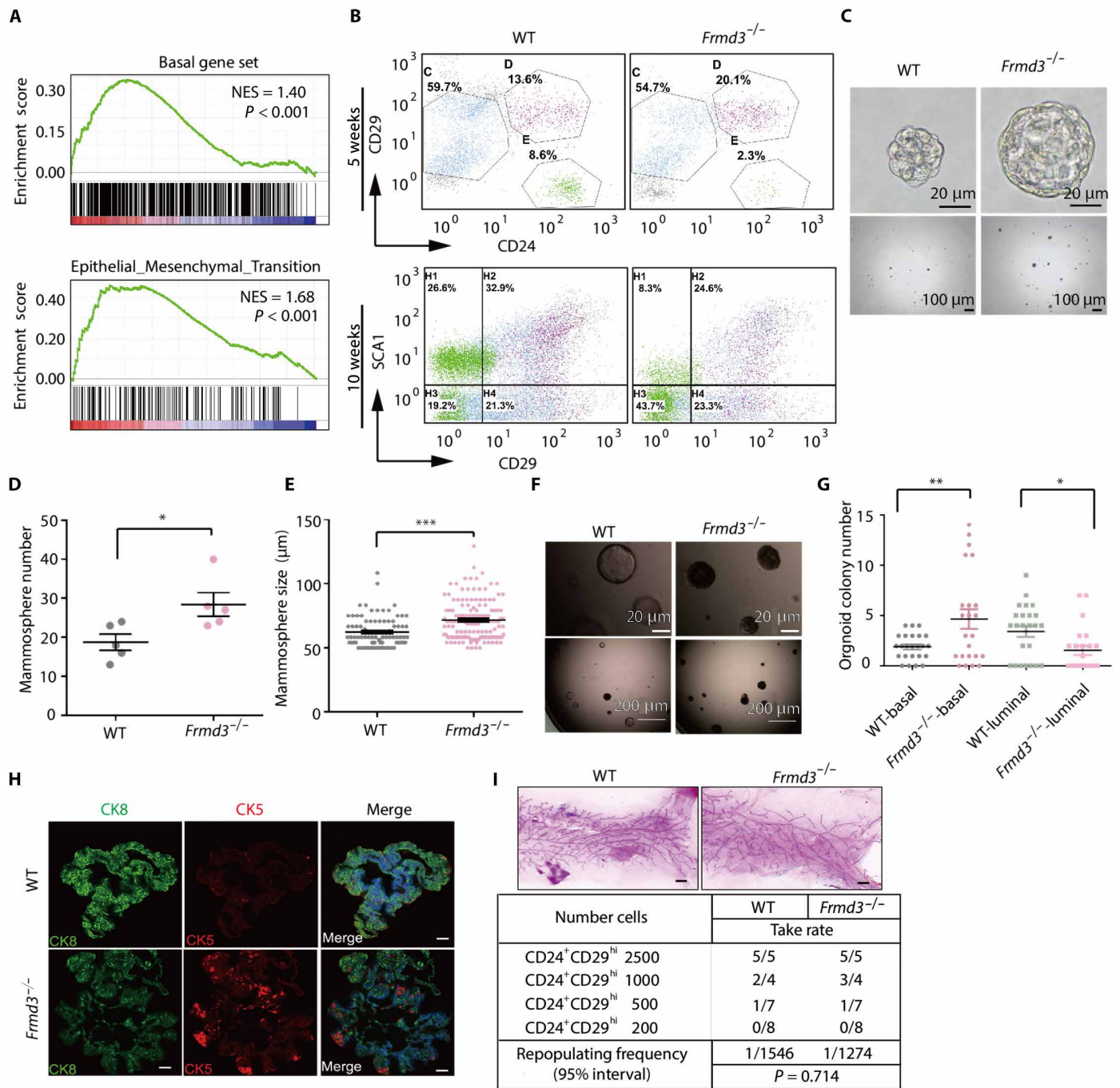
Fig. 3. Deficiency of *Frmd3* leads to the expansion of MaSCs and impairs luminal-lineage determination in MG. (**A**) Gene set enrichment analysis (GSEA) data showed the enrichment of basal gene signatures and EMT gene signatures in *Frmd3*$^{-/-}$ MG compared with WT glands. NES, normalized enrichment score. (**B**) Fluorescence-activated cell sorting analysis of CD24, CD29, and SCA1 expression in the Lin$^-$ population of MG resulting from 5- and 10-week-old virgin control and *Frmd3*$^{-/-}$ mice. (**C**) Representative images show the mammospheres generated from Lin$^-$CD24$^+$ CD29^{hi} MECs of *Frmd3*$^{-/-}$ and WT mice, and after 14-day suspension cultivation. Scale bars, 100 and 20 μm (magnified). (**D** and **E**) Quantification for mammospheres number for (C). Quantification for mammosphere sizes for (C). Only the diameter above 50 μm was counted. Data are shown as means ± SD (*n* = 5). (**F**) Representative images show the 3D morphology of MG organoids produced by *Frmd3*$^{-/-}$ and WT mice 12 days after differentiation cultivation. Scale bars, 200 and 20 μm (magnified). (**G**) The number of colonies in (F) was statistically analyzed. Data are shown as means ± SD; **P* < 0.05, ***P* < 0.01, and ****P* < 0.001, by unpaired Student's *t* test. (**H**) Representative IF staining for CK5 (red), CK8 (green), and DAPI (4′,6-diamidino-2-phenylindole; blue) in organoids generated from *Frmd3*$^{-/-}$ and WT MG. Scale bars, 100 μm. (**I**) Transplantation of sorted cells in limiting dilution. Lin$^-$CD24$^+$ CD29^{hi} cells from the MG of virgin 8-week-old *Frmd3*$^{-/-}$ and WT MG were injected into the cleared mammary fat pads of 3-week-old syngeneic recipients at the indicated cell number. Glands were collected 8 weeks after transplantation. Scale bars, 1 mm.
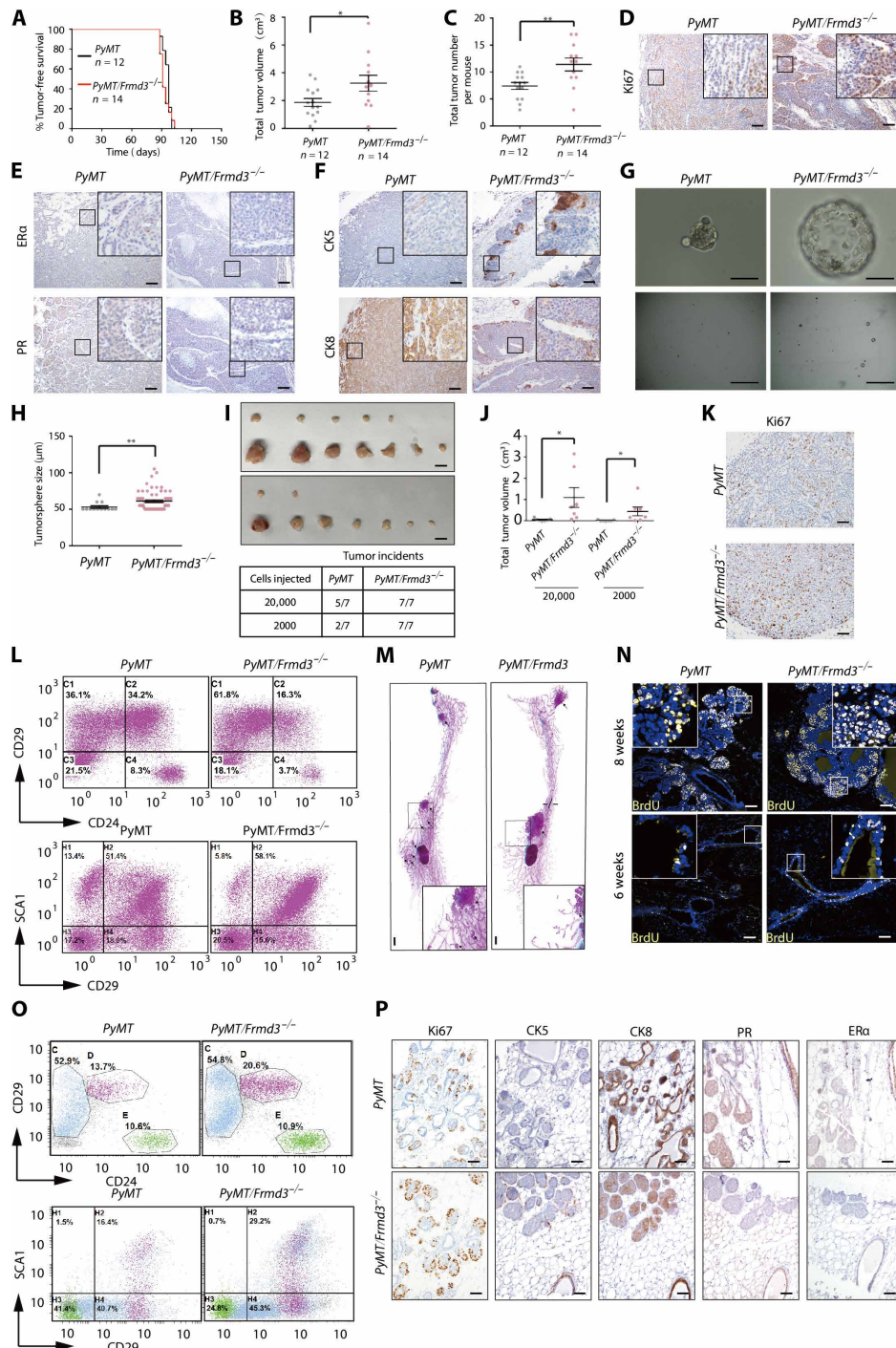
Fig. 4. Loss of *Frmd3* increases CSC stemness in *PyMT* tumors. (**A**) Kaplan-Meier survival analysis of tumor onset in *PyMT* (*n* = 14) and *PyMT/Frmd3^{−/−}* (*n* = 12) females MG. (**B** and **C**) Total tumor volumes (B) and tumor numbers (C) of *PyMT* and *PyMT/Frmd3^{−/−}* were evaluated at 120 days of age. (**D** to **F**) IHC for Ki67, ERα, PR, CK5, and CK8, in *PyMT* and *PyMT/Frmd3^{−/−}* mammary tumors at 120 days of age. Scale bars, 100 μm. (**G**) Representative picture of *PyMT* and *PyMT/Frmd3^{−/−}* tumor mammospheres after 5-day suspension cultivation. Scale bars, 200 and 20 mm (magnified). (**H**) Quantification for mammosphere sizes for (G). Only the diameter above 50 μm was counted. (**I**) Gross images of orthotopic transplantations mammary tumors. The incidence of tumors is recorded. (**J**) The volumes of tumors of each group (*n* = 7) in (I) were quantified and analyzed by single-tailed student *t* test. (**K**) IHC for Ki67 in orthotopic transplantations mammary tumor from *PyMT* and *PyMT/Frmd3^{−/−}*. Scale bars, 100 μm. (**L**) Flow cytometry analysis of Lin^− MEC purified from *PyMT* and *PyMT/Frmd3^{−/−}* mammary tumors with CD24, CD29, and SCA1 antibodies. (**M**) Representative whole-mount staining of *PyMT* and *PyMT/Frmd3^{−/−}* MG at 9 weeks of age. Scale bars, 1 μm. (**N**) Immunofluorescent staining for 5-bromo-2′-deoxyuridine (BrdU) in *PyMT* and *PyMT/Frmd3^{−/−}* hyperplastic MG and normal MG. Scale bars, 100 μm. (**O**) Flow cytometry of Lin^− MECs from MG of 6-week-old females of *PyMT* and *PyMT/Frmd3^{−/−}* mice with CD24, CD29, and SCA1 antibodies. (**P**) IHC for ER, PR, CK5, CK8, and Ki67 in *PyMT* and *PyMT/Frmd3^{−/−}* MG at 6 weeks of age. Scale bars, 50 μm. Data are shown as means ± SD; *$P < 0.05$ and **$P < 0.01$, by unpaired Student's *t* test [(A) to (C) and (H)].

cells in vivo. The tumors orthotopically transplanted from *PyMT/Frmd3*$^{-/-}$ mice had a larger volume and higher Ki67 expression compared with those from *PyMT* mice (Fig. 4, I to K). Collectively, these results indicated that deficiency of Frmd3 increases the stemness of CSCs.

We then performed flow cytometry using antibodies against CD24, CD29, and SCA1 to analyze the tumors from *PyMT* and *PyMT/Frmd3*$^{-/-}$ mice. The CD24$^+$CD29$^+$ population of *PyMT/Frmd3*$^{-/-}$ mice had lower CD24 expression and a smaller number of SCA1$^+$ cells than the CD24$^+$CD29^{Lo} population (luminal population in the normal MG) (Fig. 4L). Together, these findings indicated that Frmd3 deficiency increases the stemness of CSCs and promotes the tumor lineage transformation from luminal to basal.

The effect of *Frmd3* depletion on mammary tumors prompted us to investigate early events in tumorigenesis. The *PyMT* oncogene induced extensive hyperplasia and multiple tumor foci as early as week 4. We examined whole mounts of MGs from *MMTV-PyMT* mice at the preneoplastic stage (week 9). *Frmd3*$^{-/-}$ glands exhibited fewer but larger tumors (Fig. 4M). To explain this phenomenon, we examined proliferation in the preneoplastic MG. 5-Bromo-2′-deoxyuridine intake assay showed a marked increase in the number of proliferating cells in *PyMT/Frmd3*$^{-/-}$ MGs at weeks 6 and 8 (Fig. 4N) and a terminal deoxynucleotidyl transferase–mediated deoxyuridine triphosphate nick end labeling assay indicated enhancement of apoptosis (fig. S4A). Moreover, FACS analysis showed that *PyMT* preneoplastic tissues showed marked expansion of the LinCD24$^+$CD29^{lo} luminal subset, as reported previously (*36*). Consistently, the percentage of the Lin$^-$CD24$^+$CD29^{hi} basal population was markedly increased in preneoplastic tissues of *Frmd3*$^{-/-}$ MGs (Fig. 4O). Similarly, IHC staining of ER, PR, and CK8 was decreased and that of CK5 and Ki67 was increased in *PyMT/Frmd3*$^{-/-}$ MGs (Fig. 4P). *PyMT* oncogene-specific perturbations to the epithelial hierarchy were compromised by the loss of Frmd3. Therefore, high proliferation and a small luminal population may explain the fewer but larger tumor occurrences in *PyMT/Frmd3*$^{-/-}$ MGs.

Loss of FRMD3 increases the stemness of breast cancer cells

FRMD3 expression in breast cancer cell lines decreased concomitantly with raised tumor malignancy (Fig. 5A). We stably knocked down FRMD3 using CRISPR-Cas9 in MCF-10A human normal breast epithelial cells and overexpressed Flag-tagged FRMD3 in MDA-MB-231 human breast cancer cells. FRMD3 knockdown induced disordered polarity and mesenchymal-like morphology but did not notably influence cell migration (fig. S5, A and B), cell cycle (fig. S5C), and apoptosis (fig. S5D). To examine the inhibitory effect of FRMD3 on mammosphere formation, we used a serum-free medium cultivation system. Mammosphere formation was markedly increased in *FRMD3* knockdown cells and decreased in *FRMD3*-overexpressing cells (Fig. 5B). Furthermore, we assessed the effect of FRMD3 expression on cellular transformation by evaluating anchorage-independent growth. Soft agar colony-formation assays showed that FRMD3 overexpression inhibited colony formation (fig. S5E). Together, these findings suggested that loss of FRMD3 increases the stemness of breast cancer cells.

FRMD3 deficiency inhibits breast epithelial differentiation by inhibiting the Notch pathway

We found that Frmd3 regulates normal MaSCs and CSCs in mice, suggesting that a similar regulatory mechanism operates in human breast cells. Sox9 and ZEB1 are essential for maintaining a CSC-like state (*43*–*45*). We first examined whether Frmd3 has the same function in MCF-10A cells, which have low ERα expression. Knockdown of *FRMD3* using a short interfering RNA (siRNA) resulted in a decrease of *ESR1* expression and increased expression of *ZEB1* and *Sox9* (Fig. 5C). In MCF-7 cells, which have high ERα expression, knockdown of FRMD3 decreased the expression of ERα as well (fig. S6A).

To identify the molecular mechanism by which FRMD3 modulates stemness, we knocked down *FRMD3* in MCF-7 and T47D cells and then performed RNA sequencing (RNA-seq; GSE253455). A Kyoto Encyclopedia of Genes and Genomes (KEGG) enrichment analysis showed that the Notch pathway, a driver of luminal lineage transformation, was down-regulated (Fig. 5D). A KEGG analysis of *FRMD3*-related genes in patients with breast ductal cancer in the TCGA database confirmed this finding. The two target genes (*Hey1* and *Hes1*) of the Notch pathway were examined by knockdown of FRMD3 in MCF-7 cells (Fig. 5E), knockout of FRMD3 in mammary epithelial cells (Fig. 5F, left), and ectopic expression of FRMD3 in MDA-MB-231 cells (Fig. 5F, right). Hey1 and Hes1 levels in FRMD3 knockout mice were also detected lower than in the WT mice (Fig. 5G). These results clearly indicated that FRMD3 regulates the Notch pathway both in vitro and in vivo. To elucidate the role of FRMD3 in the Notch pathway–regulated mammosphere formation, we knocked down *FRMD3* in MCF-7 cells and then added low-dose valproic acid sodium, an activator of Notch. The result showed that without the addition of valproic acid sodium, knockdown of FRMD3 promotes mammosphere formation (Fig. 5H, left), whereas knockdown of FRMD3 could not promote mammosphere formation under the presence of valproic acid sodium that activates the Notch pathway (Fig. 5H, right). This finding indicated that the Notch pathway mediates FRMD3-regulated suppression of mammosphere formation.

We next analyzed the transcriptome of *Frmd3*$^{-/-}$ and WT luminal epithelium in the mouse MG by single-cell RNA-seq (scRNA-seq). The scRNA-seq identified four cell populations with different expression profiles in the hormone-sensitive luminal epithelium in mouse MG (Fig. 5I). Multiple volcano plots showed the genes differentially expressed (DE) in the luminal epithelial cell populations (Fig. 5J). We focused on the analyses of gene expression levels related to EMT, Notch pathway, and cell proliferation–related genes in the four cell populations. Cell populations 0 and 1 exhibited low EMT–, low proliferation–, and high differentiation–related gene expressions, suggesting the populations with highly differentiated luminal epithelial cells. Cell population 2 exhibited high EMT–, low Notch pathway–, and low proliferation–related gene expressions and also showed the lowest differentiation-related gene expression. Cell population 3 comprised well-differentiated and highly proliferative cells (Fig. 5K). Collectively, deficiency of *Frmd3* increased in the proportion of cell population 2 and decreased in cell populations 0 and 1 (Fig. 5L). Therefore, differentiation arrest of the luminal epithelial lineage caused by knockout of *Frmd3* corresponds to the inhibition of the Notch signaling pathway.

FRMD3 inhibits the Notch pathway by down-regulation of Disheveled-2

To answer how FRMD3 regulates the Notch pathway, we aim to identify proteins that interact with FRMD3. We conducted a mass spectrometry analysis of proteins pulled down by Flag-FRMD3 in MCF-7 cells. Among 907 potential interacting proteins with FRMD3, we found Disheveled-2, which is a member of the Notch pathway and
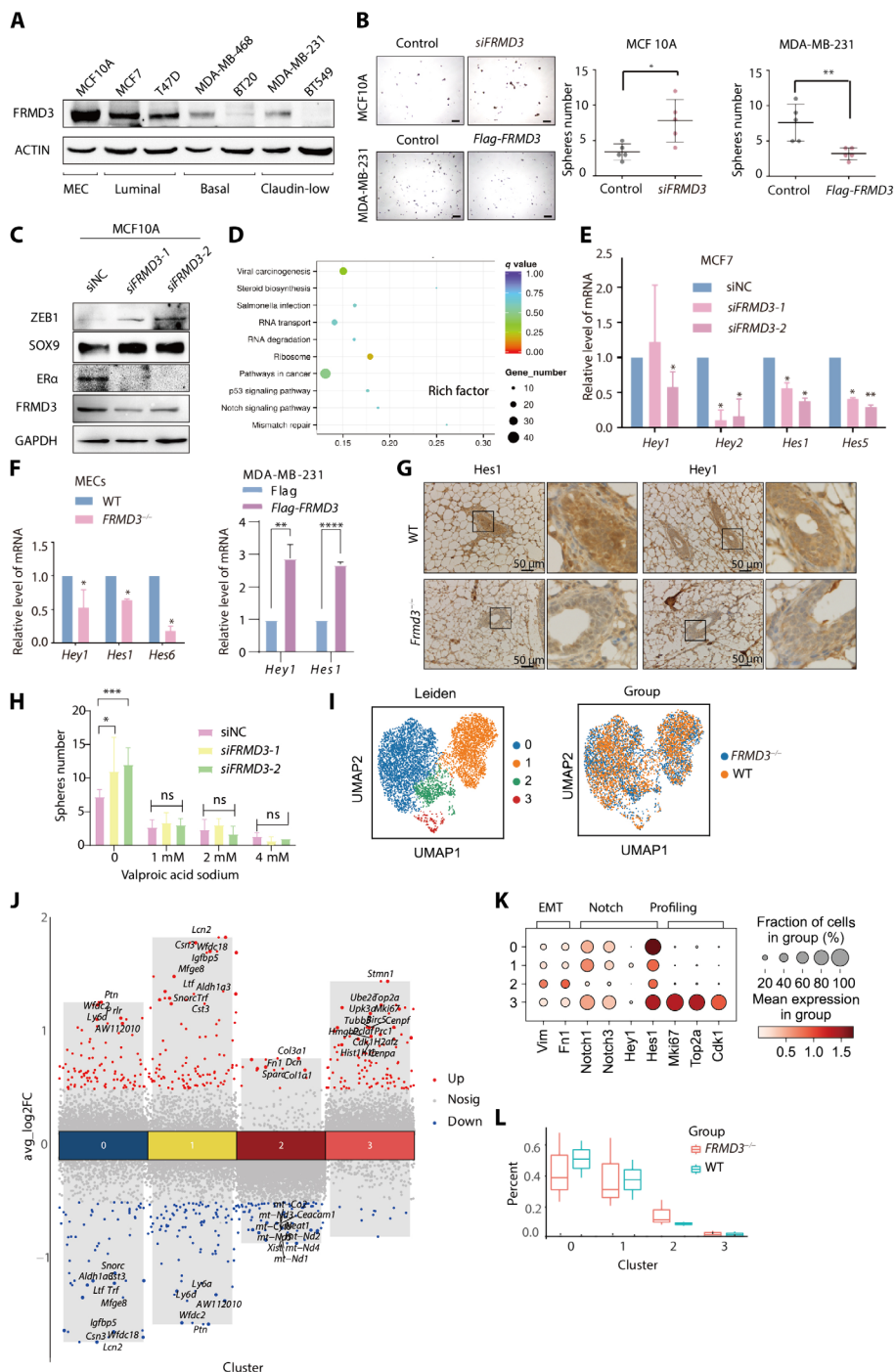
Fig. 5. FRMD3 deficiency inhibits MEC differentiation by Notch pathway inhibition. (**A**) WB analysis of FRMD3 in human MECs and breast cancer cell lines. (**B**) Representative images show the mammospheres generated from MCF-10A cells and 231 cells (left). Scale bars, 50 mm. The number of spheres was quantified with a diameter greater than 50 μm (right). (**C**) WB analysis of FRMD3, mammary marker ERα, and transcriptional factors Sox9 and ZEB1 in MCF-10A cells treated with siNC or *FRMD3* siRNA. (**D**) Top-ranked gene sets of cellular components in Gene Ontology analysis in *Frmd3*$^{-/-}$ MECs. (**E** and **F**) qPCR analysis of Notch target gene expressions in MCF-7 cells treated with control or *FRMD3* siRNAs (E), in sorted Lin$^-$ MECs populations from control and *Frmd3*$^{-/-}$ mice [(F), left], and in MDA-MB-231 cells transfected with *Flag* or *Flag-Frmd3* (F, right). The values were normalized to the housekeeping gene *GAPDH*. (**G**) IHC analysis showed Hes1 and Hey1 levels in MG of WT and *Frmd3*$^{-/-}$ mice. Scale bars, 50 μm. (**H**) Mammosphere formation assay was performed with FRMD3-knockdown MCF-7 and MCF-7 after gradient low-dose (1, 2, and 4 mM) valproic acid sodium treatment. (**I**) Uniform Manifold Approximation and Projection (UMAP) visualization of luminal epithelial cells in the single-cell RNA sequencing dataset (*n* = 4). Each dot corresponds to one single-cell–colored according to cluster (left) or group (right). (**J**) Box plots showing the proportions of luminal epithelial cell clusters in each group. (**K**) Multiple volcano plots showing genes differentially expressed (|log$_2$ fold change| > 0.5, Wilcoxon test *P* < 0.05) in each luminal epithelial cell cluster. Red dots denote up-regulated genes and blue dots denote down-regulated genes. (**L**) The expression of EMT, Notch, and proliferation-associated genes of luminal epithelial cell clusters is shown in (I). Data are shown as means ± SD; *P < 0.05, **P < 0.01, ***P < 0.001, and ****P < 0.0001 ns by unpaired Student's *t* test [(B), (E), and (F)].

related to breast cancer (Fig. 6A). The exogenous and endogenous interactions between FRMD3 and Disheveled-2 were confirmed by co-immunoprecipitation (co-IP) in human embryonic kidney (HEK) 293 T and MCF-10A cells, respectively (Fig. 6B). A glutathione *S*-transferase (GST) pull-down assay showed that Disheveled-2 interacts directly with FRMD3 via the PDZ and DEP domains in vitro (Fig. 6C). Knockdown of FRMD3 notably increased the level of Disheveled-2 in MCF-10A, MCF-7, and MDA-MB-231 cells (Fig. 6D). Western blotting (WB) showed that as the level of FRMD3 in breast tissue increases from adolescence to adulthood, the level of Disheveled-2 decreases (Fig. 6E). In addition, deletion of *FRMD3* in breast cancer cells and breast epithelial cells of gene knockout animals led to an increase of Disheveled-2 (Fig. 6F and fig. S6B). To assess the effect of Disheveled-2 on FRMD3-mediated suppression of stemness, we knocked down Disheveled-2 in FRMD3 knockdown cells and analyzed their mammosphere formation ability, breast cancer stem–like cells (CD44$^+$CD24$^-$ cells and CD133$^+$ cells), and the levels of FRMD3-regulated molecules including *Sox9* and *ZEB1*. Knockdown of Disheveled-2 reversed the enhanced mammosphere formation ability (Fig. 6G), increased the number of CD44$^+$CD24$^-$ and CD133$^+$ cells (Fig. 6G), and increased the expression of *Sox9* and *ZEB1* (Fig. 6H). *HA-FRMD3* and/or *Flag–Disheveled-2* were transfected into MCF-7 cells; *HA* and *Flag* vectors were transfected as controls. High expression of Disheveled-2 rescued the decreased mammosphere formation ability (fig. S6C). The decrease in the mRNA level of *Hey1* (a target gene of Notch signaling) caused by knockdown of FRMD3 was reversed by simultaneous knockdown of *Disheveled-2* (Fig. 6I). The increase in the *Hey1* mRNA level caused by high expression of FRMD3 was reversed by adding *Disheveled-2*; however, a nuclear-sequence mutant of *Disheveled-2(IV)* did not interfere with Notch activation by high expression of FRMD3 (Fig. 6J). Therefore, the absence of FRMD3 activates the Notch signaling pathway by increasing the level of Disheveled-2. IHC showed that the level of FRMD3 decreased and Disheveled-2 increased in breast cancer tissue compared with normal breast tissue adjacent to cancer tissue (patient 1). The lower the FRMD3 level, the higher the level of Disheveled-2 (Fig. 6K), suggesting an inverse association between the levels of FRMD3 and Disheveled-2 in human breast cancer samples.

FRMD3 promotes ubiquitin-proteasome–mediated degradation of Disheveled-2

How does FRMD3 deficiency increase the level of Disheveled-2? We first excluded the FRMD3 regulation of Disheveled-2 at the gene transcriptional level (fig. S7A). We then found that overexpression of FRMD3 shortened the half-life of Disheveled-2 in MDA-MB-231 cells (Fig. 7, A and B) and knockdown of FRMD3 prolonged the half-life of Disheveled-2 in MCF-10A cells (fig. S7B). The addition of MG132, but not CQ, to Sum159 and MCF-10A cells reversed the decreased Disheveled-2 level caused by overexpression of FRMD3 (Fig. 7, C and D). Furthermore, in MDA-MB-231 and HEK-293T cells, *GFP-FRMD3* and *C-Myc–FRMD3* increased the ubiquitination level of Disheveled-2 (Fig. 7E, left and middle), whereas knockdown of *FRMD3* by siRNA reduced its ubiquitination level (Fig. 7E, right). The above results demonstrated that FRMD3 promotes the degradation of Disheveled-2 via the ubiquitin-proteasome mediated pathway. How does FRMD3 interact with Disheveled-2 and promote its degradation? We found that the binding of Disheveled-2 to its deubiquitinase USP9x was weakened by ectopic expression of FRMD3 (Fig. 7F). In MCF-10A cells, knockdown of USP9x

abolished the up-regulation of Disheveled-2 caused by depletion of *FRMD3* (Fig. 7G). This indicates that FRMD3 promotes the degradation of Disheveled-2 via the ubiquitin-proteasome pathway by inhibiting its binding to the deubiquitinase USP9x. Thus, FRMD3 deficiency caused inhibition of the Notch signaling pathway is achieved by preventing ubiquitin-proteasome mediated degradation of Disheveled-2. Although Disheveled-2 is also a member of the β-catenin destroy complex, we did not detect remarkable β-catenin nuclear translocation or activation of the Wnt signaling pathway after knockdown of FRMD3 in MCF-10A cells (fig. S7, C to E).

FRMD3 inhibits the phosphorylation and nuclear location of Disheveled-2

Because the entry of Disheveled-2 into the nucleus is required for its inhibition of the Notch signaling pathway, does the absence of FRMD3 promote the entry of Disheveled-2 into the nucleus? To this end, we performed immunofluorescence (IF) labeling of Disheveled-2 (red) and Hey1 (green) in the mammary ductal epithelium of *Frmd3*$^{-/-}$ and WT mice. The results indicated that *Frmd3* knockout not only increases the level of Disheveled-2 and reduces the level of Hey1 in breast ductal epithelial cells (Fig. 8A) but also significantly increases the amount of Disheveled-2 entering the nucleus (Fig. 8B). Next, we knocked down *FRMD3* in MCF-10A, MCF-7, and MDA-MB-231 cells followed by IF staining. The result showed an increased nuclear localization of Disheveled-2 (Fig. 8C).

Nuclear and cytoplasm separation experiments confirmed that the amount of Disheveled-2 in the nuclei was increased by knockdown of FRMD3 and decreased by ectopic expression of FRMD3 (Fig. 8D), suggesting that the absence of FRMD3 promotes entry of Disheveled-2 into the nuclei. The phosphorylation of Disheveled-2 by CKs promotes its binding to the nuclear entry-helper molecule FOXKs. However, whether FRMD3 plays a role in the regulation of Disheveled-2 phosphorylation is unknown. To this end, we found that high expression of *HA-FRMD3* leads to a decrease in the phosphorylation level of Flag–Disheveled-2 in MDA-MB-231 cells (fig. S8) and knockdown of FRMD3 using an siRNA increased the phosphorylation level of Flag–Disheveled-2 in MCF-7 cells (Fig. 8E), indicating that FRMD3 inhibits the phosphorylation of Disheveled-2. Mass spectrometry analysis showed that the key FRMD3-regulated phosphorylation site in Disheveled-2 is S155 (Fig. 8F). Ectopic expression of *HA-FRMD3* in MDA-MB-231 cells reduced the interactions of Disheveled-2 with CK1 and FOXKs (fig. S8). By contrast, the knockdown of *FRMD3* by siRNA in HEK-293T cells promoted their interactions (Fig. 8G). This finding indicates that FRMD3 suppresses the phosphorylation of Disheveled-2 by inhibiting the interaction of Disheveled-2 with CK1, thereby inhibiting the interaction of Disheveled-2 with FOXKs and consequently preventing nuclear entry of Disheveled-2. Disheveled-2 inhibits the Notch signaling pathway by binding to the Notch intracellular domain (NICD) after entry into the nucleus, thereby suppressing the transcription of Notch downstream target genes. As expected, FRMD3 exerted a blocking effect on Disheveled-2 and inhibited its binding to NICD (Fig. 8G). We transfected different fragment constructs of *Flag-FRMD3* into HEK-293T cells and then performed co-IP assay. The result showed that the FERM domain is required for FRMD3 binding to Disheveled-2, FOXK2, and CK1 (Fig. 8, H to J). We further evaluated the level of p-Disheveled-2 in WT and *Frmd3*$^{-/-}$ MGs of weeks 8 and 12 in mice by IHC. The level of p-Disheveled-2 was increased in *Frmd3*$^{-/-}$ MECs compared to the WT MECs. From weeks 8 to 12, the amount of p-Disheveled-2 in the
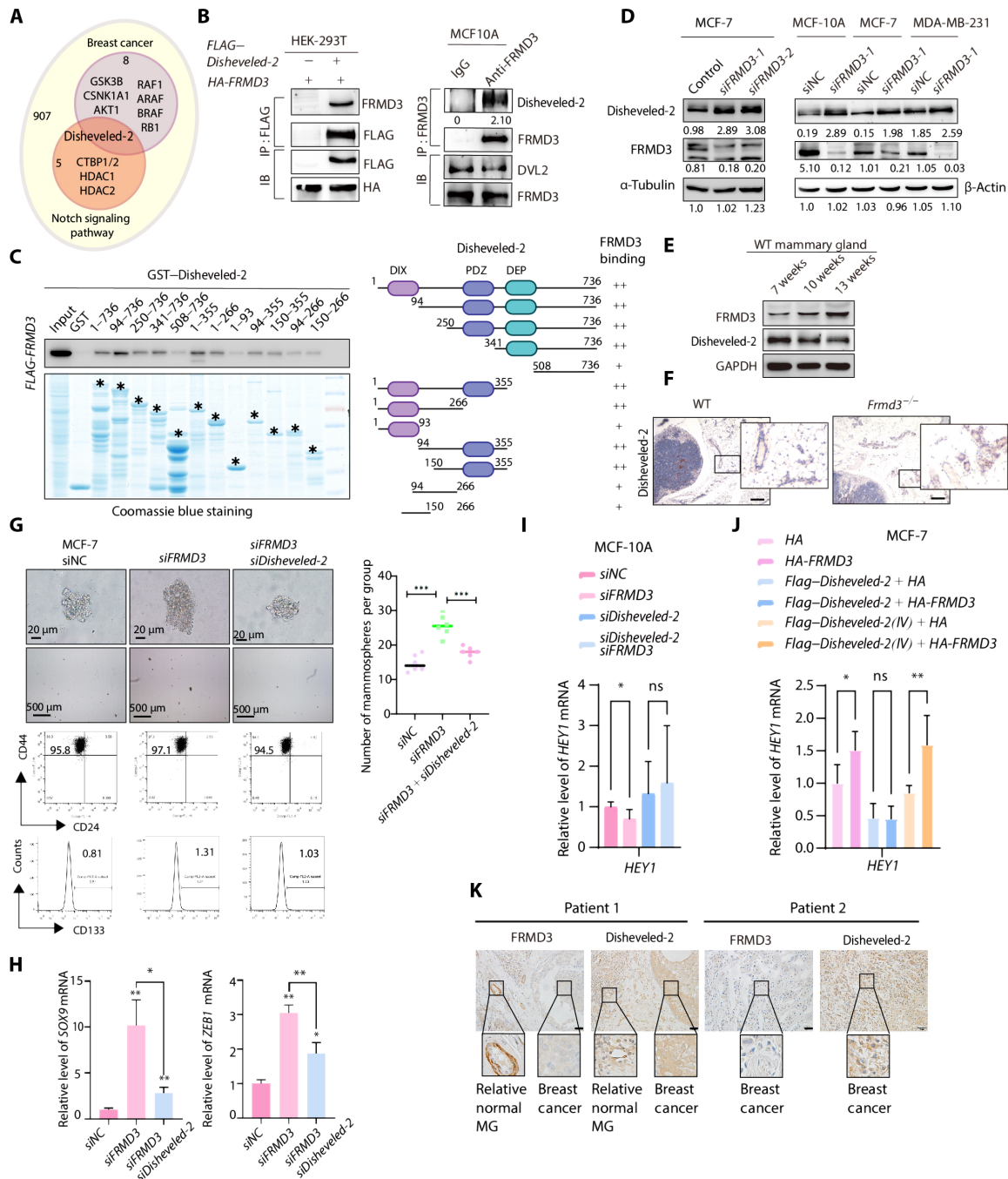
Fig. 6. FRMD3 activates the Notch signaling pathway by down-regulation of Disheveled-2. (**A**) Immunoprecipitation (IP) with Flag-FRMD3 in MCF-7 cells and the mass spectrometry was performed to find potentially interacting proteins with FRMD3. (**B**) Human embryonic kidney (HEK) 293A cells were transfected with *HA-FRMD3* with or without *Flag–Disheveled-2*. IP was performed with M2 beads followed by WB with the indicated antibodies (left). The endogenous interaction between FRMD3 and Disheveled-2 was analyzed by co-IP in MCF-10A cells with control IgG or FRMD3 antibody followed by WB with the indicated antibodies (right). (**C**) Glutathione *S*-transferase (GST) or GST–Disheveled-2 truncated proteins were subjected to WB (left). Schematic illustration of human Disheveled-2 protein domains and region required for FRMD3 binding (right). (**D**) WB for FRMD3 and Disheveled-2 protein levels in MCF-10A, MCF-7, and MDA-231 cells treated with control or *FRMD3* siRNA. (**E** and **F**) Frmd3 and Disheveled-2 were detected by WB in WT MG at different stages and by IHC in *Frmd3*$^{-/-}$ and WT MG. Scale bars, 50 μm. (**G**) *FRMD3* siRNA and/or *Disheveled-2* siRNA were transfected into MCF-7 cells with consiRNA as control. Top: Representative images showed the mammospheres generation (4000 cells/ml). The number of spheres was quantified with a diameter greater than 50 μm. Six scopes pre-group. Middle: Representative CD24/CD44 and CD133 flow cytometric profiles showed the CSC population (CD44$^+$ CD24$^-$ or CD133$^+$). (**H**) qPCR was adopted to analyze the FRMD3-regulated gene *Sox9* and *ZEB1* mRNA level. (**I**) *FRMD3* siRNA and/or *Disheveled-2* siRNA were transfected into MCF-10A cells with con siRNA as control. qPCR was adopted to analyze the *Hey1* mRNA level. (**J**) *HA-FRMD3* with or without *Flag–Disheveled-2 + HA/Flag–Disheveled-2(IV)* were transfected into MCF-7 cells. qPCR was adopted to analyze the *Hey1* mRNA level. (**K**) FRMD3 and Disheveled-2 were detected by IHC in human breast cancer tissues. Scale bars, 50 μm. Data are shown as means ± SD (Student's *t* test); *$P < 0.05$ and **$P < 0.01$ [(G) to (J)].
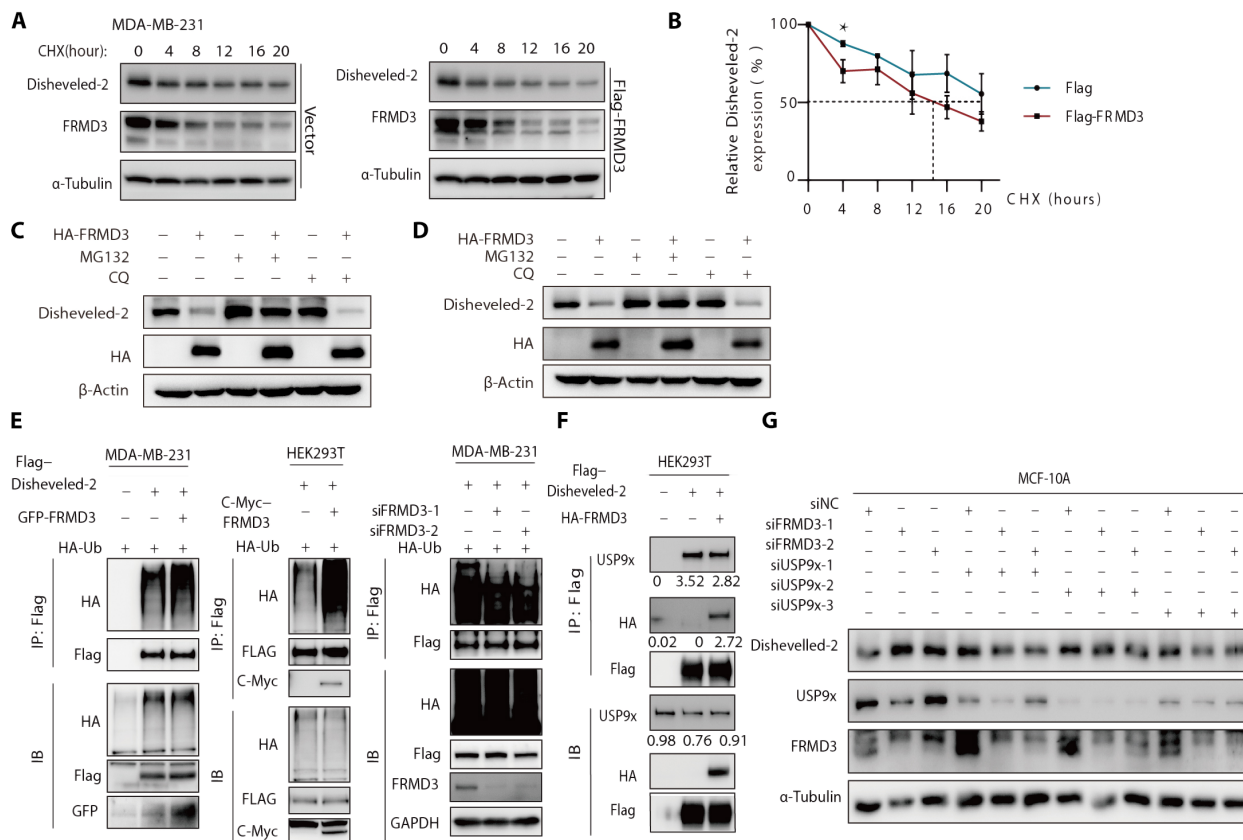
Fig. 7. FRMD3 promotes ubiquitin-proteasome mediated degradation of Disheveled-2. (**A**) Lysates from MDA-MB-231 cells overexpressing *Flag* or *Flag-FRMD3* treated with cycloheximide (CHX; 100 μg/ml) for the indicated times were subjected to WB with indicated antibodies. (**B**) Disheveled-2 protein levels were quantified by normalizing to the intensity of the α-tubulin band (three independent experiments). (**C** and **D**) WB analysis of Disheveled-2 in WT and FRMD3-high expression MCF-10A cells (C) and in WT and FRMD3-high expression MDA-MB-231 cells (D). The cells were treated with MG132 (25 μM) or CQ (50 μM) for 6 hours before harvest. (**E**) WT- and FRMD3-overexpressed MDA-MB-231 cells (left), and HEK-293 T cells (middle), and WT and FRMD3 knockdown MDA-MB-231 cells (right) were cotransfected with *Flag–Disheveled-2* and HA-Ub as indicated. Whole-cell lysate was immunoprecipitated with anti-Flag and then Western blotted for ubiquitinated Disheveled-2. (**F**) Lysates of MCF-10A cells cotransfected with *Flag–Disheveled-2* and *HA-FRMD3* as indicated were immunoprecipitated with anti-Flag and then Western blotted for endogenous USP9x. (**G**) WB analysis of Disheveled-2 levels in WT and FRMD3 knockdown MCF-10A cells combining with or without *USP9x* knockdown.

mouse MG decreases with the increasing expression of FRMD3. These findings suggested that FRMD3 inhibits the phosphorylation of Disheveled-2 endogenously (Fig. 8K).

DISCUSSION

During breast development, the maintenance and differentiation of breast stem cells are regulated by multiple signaling pathways; among them, the Notch signaling pathway maintains the luminal lineage plasticity (*18*, *46*). In this study, the FERM domain protein FRMD3 was found to regulate the plasticity of breast epithelial cells and to be necessary for the differentiation of breast stem cells into luminal lineages. Deficiency of Frmd3 enhanced the stemness and impaired the differentiation and tumorigenesis of breast epithelial cells. FRMD3 destabilizes Disheveled-2 and inhibits Disheveled-2 interaction with its deubiquitinase UPS9x. In addition, FRMD3 inhibits Disheveled-2 interaction with CK1 to inhibit its phosphorylation. FRMD3 also inhibits the nuclear translocation of Disheveled-2 by inhibiting its interaction with the entry-helper protein FOXK1/2. FRMD3 relieves the restriction of Disheveled-2 on the Notch signaling pathway by inhibiting the interaction of Disheveled-2 with NICD (Fig. 9). Collectively,

FRMD3 activates the Notch signaling pathway, promoting the luminal differentiation of breast stem cells. Our findings demonstrated a regulatory mechanism for FRMD3–Notch signaling that controls MEC fate decisions and also extended our understanding of the origin and occurrence of TNBC.

It has been speculated that breast cancer arises from the accumulation of oncogenic hits in a genetically normal precursor and that different oncogenic signaling pathways target different cells of origin, leading to the formation of the various subtypes of breast tumors. For example, depletion of *BRCA1/2* in any of the tested cell populations initiated basal-like tumors, and deletion of *Lfng or ΔNp63* in the luminal population induced or attenuated basal-like tumor formation (*47*–*49*). Loss of p53 facilitated the acquisition of MaSC-like properties by luminal cells and predisposed them to claudin-low breast cancer (*50*). Expression of the *PIK3CA* mutant in basal or luminal cells evoked cell dedifferentiation into a multipotent stem–like state and induced multilineage mammary tumors (*51*). In this study, the Frmd3 expression level in the MG gradually increased from puberty to maturity, which is similar to the expansion of the luminal population, suggesting a correlation between FRMD3 and luminal cell formation. *Frmd3*^{−/−} mice MG underwent
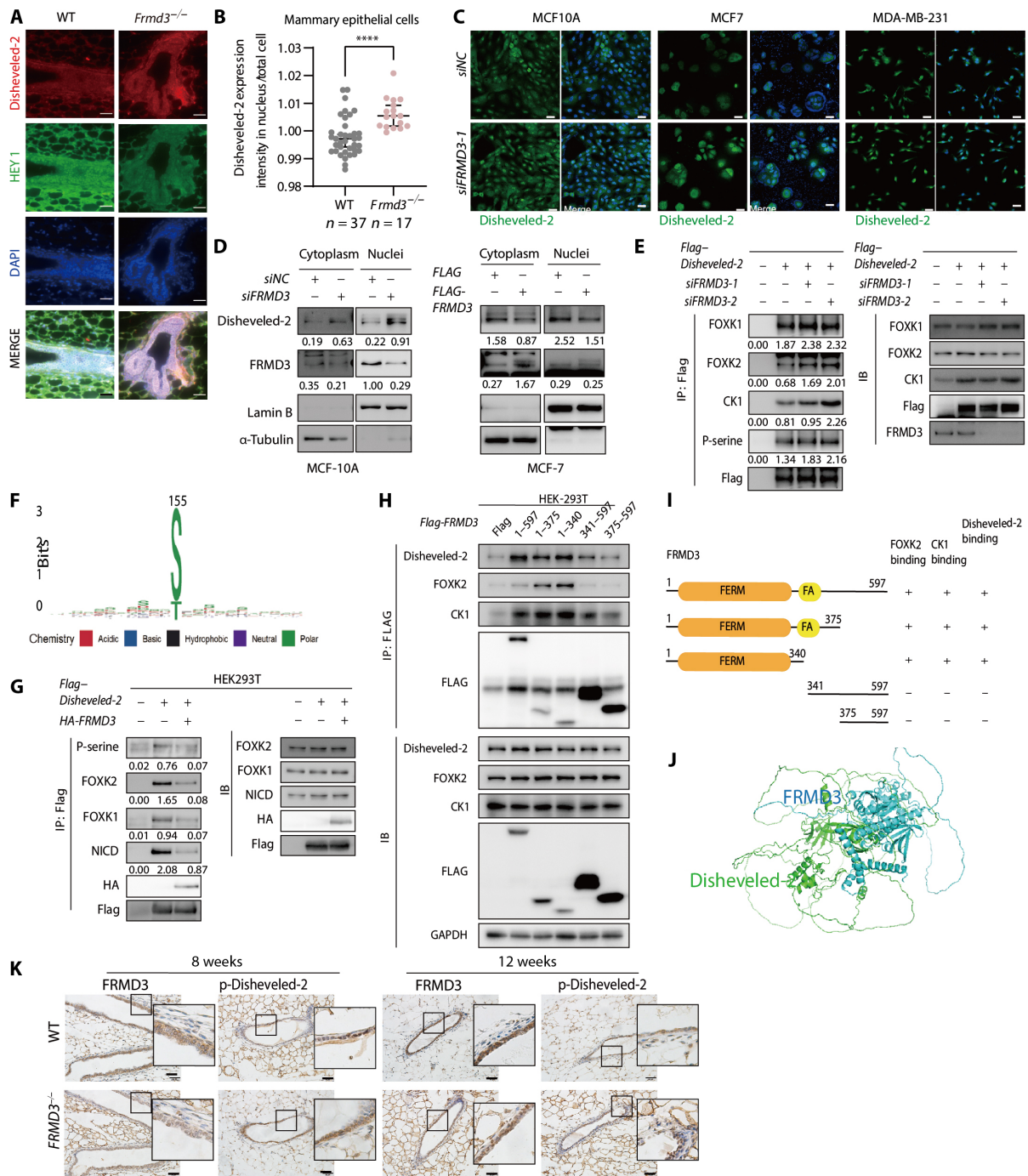
Fig. 8. FRMD3 inhibits the phosphorylation and nuclear localization of Disheveled-2. (**A**) Representative multiplex IF images of MEC of *Frmd3*$^{-/-}$ mice and WT mice. Scale bars, 50 μm. (**B**) Quantification of Disheveled-2 intensity in nucleus per total cell in MECs of *Frmd3*$^{-/-}$ mice ($n = 17$) and WT mice ($n = 37$). Data are shown as means ± SD, ****$P < 0.00001$, by unpaired Student's *t* test. (**C**) IF images of Disheveled-2 in WT or *FRMD3* knockdown MCF-10A, MCF-7, and MDA-MB-231 cells, respectively. Scale bars, 50 μm. (**D**) Disheveled-2 and FRMD3 were detected in nuclear and cytoplasmic fractions of MCF-10A knocking down *FRMD3* or not (left) and of MCF-7 overexpression of *FRMD3* or not (right). YY1 was used as a nuclear internal control, and α-tubulin was used as a cytoplasm internal control. (**E**) MCF-7 cells were cotransfected with *Flag–Disheveled-2* and *siFRMD3*. co-IP assays were performed using cell lysates with flag antibodies. WB was performed with indicated antibodies. (**F**) Liquid chromatography–tandem mass spectrometry analysis of the spectrum of the charged ion [mass/charge ratio (*m/z*) 955.47791] indicated that S155 was phosphorylated when *FRMD3* was knocked down. (**G**) HEK-293 T cells cotransfected with *Flag–Disheveled-2* and *c-Myc–FRMD3* or *HA-FRMD3*, and co-IP assays were performed using cell lysates with flag antibodies. WB was performed with indicated antibodies. (**H**) Flag-tagged various *FRMD3* truncations were transfected into HEK-293 T cells. Co-IP assays were performed using cell lysates with flag antibodies. Disheveled-2, FOXK2, and CK1 were detected by WB. (**I**) Schematic illustration of human FRMD3 domains and regions required for binding with Disheveled-2, FOXK2, or CK1. (**J**) Binding pattern of FRMD3 and Disheveled-2. (**K**) FRMD3 and p-Disheveled-2 were detected by IHC in *Frmd3*$^{-/-}$ and WT MG. Scale bars, 20 μm.
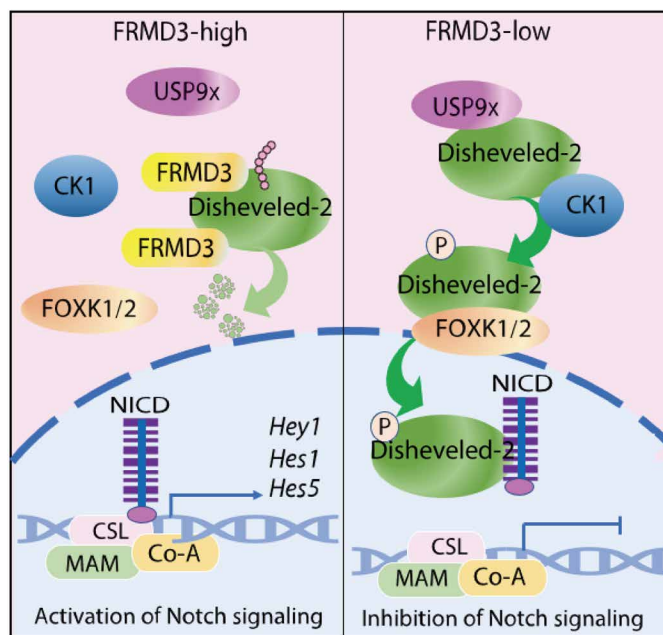
Fig. 9. Working model. The mechanism of FRMD3 promotes the degradation of Dishevedled-2 and activates the Notch signaling pathway.

a luminal to basal transition and *MMTV-PyMT/Frmd3$^{-/-}$* mice MG exhibited accelerated tumor progression. In vitro functional assays confirmed the tumor-suppressive effect of Frmd3. On the basis of triple-negative tumors, premalignant lesions, normal MGs, and MEC populations, we showed that Frmd3 controls MaSC self-renewal and maintains the formation of the normal luminal lineage. Also, deficiency of Frmd3 is an oncogenic hit, and loss of Frmd3 leads to a disordered hierarchy of MECs, thereby inducing malignant transformation and facilitating the development of TNBC.

Previous studies reported that both Wnt and Notch are classical signaling pathways in regulating MaSC fates. Wnt proteins and the LRP5 receptor are essential for maintaining MaSCs and the basal cell lineage (*46*, *52*). Disheveled-2 serves as a bracket and recruits β-catenin disruption complex components to the Wnt receptor Frizzled-LRP5/6, causing the disruption complex to lose activity and preventing phosphorylation of substrates (including β-catenin) by GSK-3β. Having escaped degradation, β-catenin accumulates in the cytoplasm and nucleus; in the end, it binds to the transcription factor complex formed by Tcf/Lef, activating multiple important target genes (*53*). Disheveled-2 was reported to activate the Wnt signaling pathway, but in the present study, the knockdown of FRMD3 did not notably induce β-catenin nuclear translocation or activate the Wnt signaling pathway (fig. S7, E and F). The specific reason is unclear, but it cannot be ruled out that the increase in Disheveled-2 caused by FRMD3 deficiency mainly exerts Notch inhibition via entering into the nucleus, which leads to a less increasing effect on β-catenin in the cytoplasm. Irrespective of the mechanism, we showed that FRMD3 is a specific inhibitor of the Notch signaling pathway in this study.

As a scaffold protein, FRMD3 interacts with a variety of proteins to influence signal transduction. In this study, mass spectrometry analysis showed that FRMD3 physically interacts with Disheveled-2 and knockdown of FRMD3 increased Disheveled-2 level in the nuclei; these findings were confirmed in mouse MGs. Disheveled-2 suppresses Notch signaling by inhibiting *CSL* (*54*, *55*), and *Sox9* is suppressed by the Notch pathway (*56*, *57*). Unexpectedly, FRMD3 deficiency

inhibited the Notch pathway and up-regulated Sox9 expression. MaSC population expansion, the impaired luminal lineage formation, and the transient overgrowth in mammary ductal morphogenesis during early puberty in *Frmd3$^{-/-}$* mice are similar to a mouse model of the Notch signaling pathway suppression (*18*, *33*, *46*, *58*, *59*). Therefore, we presented a hypothesis that the FRMD3–Disheveled-2–Notch axis maintains the MEC hierarchy and explains the phenotype of FRMD3-deficient mice. However, mice with high expression of Disheveled-2 and the corresponding phenotype were not established in this study, which makes it impossible for us to demonstrate in vivo that *Frmd3* deletion inhibits the notch signaling pathway by upregulating Disheveled-2. For this in vivo confirmation, future investigation will be taken.

FRMD3 expression was low in breast cancer, which is strongly associated with a poor prognosis in the patients. Therefore, FRMD3 may play an important role in breast progression. Methyltransferase inhibitor 5-AZA-dC increased the *FRMD3* mRNA and FRMD3 protein levels (Fig. 1, I and J), indicating that the *FRMD3* promoter is methylated by a DNA methyltransferase. The highly expressed DNA methyltransferases in breast cancer are DNMT1, DNMT3A, and DNMT3B, which are also common targets of clinical demethylation therapy (*60*). These methyltransferases may also be responsible for the low expression of FRMD3 in patients with breast cancer. In summary, we demonstrated that FRMD3 is a tumor-suppressive protein that controls the luminal-to-basal transformation and the stemness of breast cancer cells by activation of the Notch signaling pathway.

MATERIALS AND METHODS
TMA IHC analysis
IHC for FRMD3 in human breast cancer tissue microarray (TMA; HBr-Duc140Sur-01) was performed. Immunostained microarrays were scored by two pathologists blind to cancer outcomes. According to histological scoring, the reactivity of staining was ranked into four grades: no reactivity (score = 0), faint reactivity (score = 1), moderate

reactivity (score = 2), and strong reactivity (score = 3 or 4). The general situation and FRMD3 expression level of patients with breast cancer in the TMA were summarized in table S1. All human tissues used in this study were approved by the Ethics Committee of Sino-Japan Friendship Hospital, Beijing, China, with permit number ZRLW-5. All procedures were in accordance with the ethical standards of the responsible committee on human experimentation (institutional and national) and the Helsinki Declaration of 1975, as revised in 2000(5). Informed consent was obtained from participants, in accordance with approval of the local ethical committee.

Mice

The knockout C57BL/6J mice for *Frmd3* were generated using CRISPR-Cas9–based targeting and nonhomologous end joining. In founder lines, genotyping on genomic DNA from mouse tails was verified by multiplex polymerase chain reaction (PCR) to obtain *Frmd3*$^{-/-}$ mice, which were further intercrossed to yield healthy offspring. The *MMTV-PyMT* (*FVB/N*) strain was originally obtained from Z. Yu's laboratory and was backcrossed for seven generations to C57BL/6 background. WT C57BL/6 mice were provided by the animal facility of the Peking University Health Science Center. Mice were housed in a pathogen-free animal facility at the Laboratory Animal Center of Peking University Health Science Center with a 12-hour light/dark cycle, constant temperature and humidity, and fed with standard rodent chow and water ad libitum. All animal experiments were approved by the Peking University Biomedical Ethics Committee and the approval number is BCJB0102. Genomic DNA extracted from mouse tail biopsies was subjected to standard genotyping PCR. The reaction conditions were 5 min at 94°C; 35 cycles of 30 s at 94°C, 30 s at 60°C, and 1 min at 72°C followed by 5 min at 72°C and hold at 4°C.

Histology, whole-mount staining, and immunostaining

Murine mammary tissue samples were fixed in 10% formalin, paraffin-embedded, and sectioned (5 μm) for immunostaining or fixed in Carnoy's fixative (6:3:1, 100% ethanol:chloroform:glacial acetic acid), rinsed through graded alcohol followed by distilled water, then stained in carmine alum xylene and mounted with Permount. For IHC and IF staining, sectioned samples were immunostained according to the standard protocols: deparaffinization, antigen-retrieval, hydrogen peroxide treatment or Triton X-100 treatment, blocking, incubation with primary and secondary antibodies, and counterstained with 4′,6-diamidino-2-phenylindole.

Mammary cell preparation, FACS analysis, and cell sorting

MGs were collected from 5- to 10-week-old virgin female mice and the minced tissue was placed in culture medium (DMEM/F12 and Hepes), collagenase (300 U/ml), and hyaluronidase (100 U/ml) for 3 to 6 hours at 37°C. After lysis of the red blood cells with NH$_4$Cl, a single-cell suspension was obtained by sequential dissociation of the fragments in 0.25% trypsin-EDTA for 1 to 2 min and dispase (5 mg/ml) plus deoxyribonuclease I (0.1 mg/ml; Sigma-Aldrich) for 2 min with gentle pipetting, followed by filtration through 40-μm cell strainer (BD Falcon). Cell sorting was performed on the Gallios Flow Cytometer (Beckman Coulter) and FACSCalibur. FACS data were analyzed by FlowJo software.

Cell culture and viral infection

In this study, eight cell lines were used including MCF-10A, MCF-7, T47D, MDA-MB-231, MDA-MB-468, BT20, BT549, and HEK-293T. The detailed species information, supplier name, catalog number, and culture condition are listed in table S2. Lentivirus was produced in HEK-293 T cells and cotransfected with pMD, pSPAX, and target gene expression vector. Virus-infected cells were selected with puromycin.

Transwell migration assay and soft agar assay

For Transwell migration assays using MCF-10A and MDA-231 cells, 5×10^4 cells were plated on 8-μm Transwell filters (Corning). The cells were induced to migrate toward a medium containing 20% fetal bovine serum (FBS) for 20 hours (for migration assay) in the CO$_2$ incubator. Non-invading cells were removed with a cotton swab. The remaining cells were fixed, stained with H&E, and analyzed by a bright-field microscope. Ten random fields were chosen, and cell numbers were averaged (*35*).

Sphere formation, organoid culture, and mammary fat pad transplantation assays

For sphere culture, sorted Lin$^-$CD24$^+$CD29^{hi} basal cells or digested single tumor cells were seeded in a six-well ultralow attachment plate in DMEM/F12 medium containing B27 supplement, epidermal growth factor (EGF; 20 ng/ml), fibroblast growth factor (20 ng/ml), and heparin (4 μg/ml) and cultured for 5 to 14 days. For organoid culture, sorted Lin$^-$ MECs were embedded in Matrigel (BD Pharmingen) in a 96-well ultralow attachment plate covered with DMEM/F12 medium supplying 10% FBS, insulin (5 μg/ml), hydrocortisone (1 μg/ml), cholera toxin (10 ng/ml), EGF (10 ng/ml) and cultured for 10 to 14 days. For transplantation assay, sorted cells were resuspended in 50% Matrigel, phosphate-buffered saline (PBS) with 20% FBS, and 0.04% trypan blue (Sigma-Aldrich) and injected in 10-μl volumes into the cleared fat pads of a 3-week-old female. Reconstituted MGs were harvested after 8 weeks after surgery. Outgrowths were detected after carmine staining which more than 10% of the host fat pads filled were scored as positive.

Plasmids and siRNAs

The *HA*-tagged *FRMD3*, *Flag*-tagged *FRMD3*, and *Flag*-tagged *Disheveled-2* expression plasmids were constructed by cloning PCR-amplified sequences into an N-terminal HA-tag pcDNA3.1 vector and N-terminal 3× FLAG vector (Sigma-Aldrich). The CRISPR guide RNA against *FRMD3* was designed by the Zhang Lab website and cloned in the lentiCRISPRv2 vector. All constructs were confirmed by DNA sequencing. Three siRNAs targeting human *FRMD3* were designed and synthesized by RiboBio. The sense-targeting sequences were as follows: sequence 1, 5′- GGGAAAUAAGAGAAUCCAUdTdT-3′; sequence 2, 5′- GCUGC-CUGCAAACAUCUUUdTdT-3′; and sequence 3, 5′-GGUGCACAG-AGCCAACAUUdTdT-3′. An irrelevant double-stranded RNA with the sense sequence 5′-UUCUCCGAACGUGUCACGU-3′ was used as control. siRNAs targeting human *Disheveled-2*: sequence 1, 5′-AGGU-UCAGCAGCUCCACGGATT-3′; sequence 2,5′-UCCGUGGAGCU-GCUGAACCUTT-3′

Antibodies

The following antibodies were used: Flag (Sigma-Aldrich), HA (Sigma-Aldrich), FMRD3 (Sigma-Aldrich), Disheveled-2 (3224, CST), K5 (ab53121, Abcam), K14 (PRB-155P, Covance), K8 (TROMA-1, DSHB), α-SMA (ab5694, Abcam), ERα (1:500; sc-542, Santa Cruz Biotechnology Inc.), PR (Santa Cruz Biotechnology Inc.), HER2 (Santa Cruz Biotechnology Inc.), Ki67 (MA5-14520, Thermo Fisher

Scientific), E-cadherin (CST), Claudin 3 (SAB4200758, Sigma-Aldrich), Vimentin (5741, CST), Anti-mouse CD31 (BD PharMingen), Anti-mouse CD45 (BD PharMingen), Anti-mouse Ter119 (BD PharMingen), Anti-mouse CD24 FITC (110242, ebioscience), Anti-mouse CD29 PE (120291, ebioscience), Anti-mouse CD49f PE (120495, ebioscience), Anti-mouse CD61 APC (104315, ebioscience), Anti-mouse CD49b APC (17597163, ebioscience), and Anti-mouse Sca1 APC (17598182, ebioscience). Detailed information on antibodies is listed in table S3.

Immunoprecipitation and WB analysis
Cells were lysed in NP-40 buffer [50 mM tris-HCl (pH 7.4), 150 mM NaCl, 1% NP-40, 1 mM EDTA, and 10 mM sodium butyrate] containing protease inhibitors. Co-IP was performed using indicated primary antibodies and protein A/G agarose beads (Santa Cruz Biotechnology Inc.) or anti-Flag M2 beads (Sigma-Aldrich) at 4°C. Then, immune complexes were washed for extended times with radioimmunoprecipitation assay buffer and separated by SDS–polyacrylamide gel electrophoresis gels. Transfer membranes were probed with indicated primary and secondary antibodies. The membranes were detected by the Super Signal Chemiluminescence Kit (Thermo Fisher Scientific).

Orthotopic transplantations of mammary tumors
Quantitative number of tumor cells from *PyMT* and *PyMT/Frmd3*$^{-/-}$ mice, 20,000 cells per mouse or 2000 cells per mouse were injected into the cleared mammary fat pads of 3-week-old syngeneic recipients, and tumors were collected 9 weeks after transplantation. The incidence of tumors is recorded.

RT-qPCR analysis
Total RNA was isolated from cells using TRIzol reagent (Invitrogen). The first chain cDNA was synthesized using HiScript II Q RT SuperMix for quantitative PCR (+gDNA wiper, Vanzym, China). Reverse transcription PCR (RT-PCR) analyses were performed on the LightCycler 96 detection system (Roche) using the Power SYBR green PCR master mix (Applied Biosystems) according to the manufacturer's instructions. All mRNA expression levels were normalized to the signal of the *GAPDH* gene. The gene-specific primer sets were used at a final concentration of 0.1 μM and their sequences are listed in table S4.

GST pull-down assay
GST-tagged various Disheveled-2 truncations were purified and incubated with HEK-293 T lysates which were transiently transfected with *Flag-FRMD3*. Pull-down assays were performed with Sepharose 4B protein beads. FRMD3 proteins in HEK-293T pulled down by GST or GST–Disheveled-2 truncated proteins were subjected to WB analysis.

Subcellular fractionation
Cells were washed twice with PBS and scraped into buffer A [10 mM Hepes (pH 7.9), 10 mM KCl, 0.1 mM EDTA, 0.1 mM EGTA, 1 mM DTT, and 0.15% NP-40]. The cell suspension in this lysis buffer was incubated on ice for 20 min to allow swelling. The cells were then centrifuged at 13,000 rpm for 10 s, and the cytosol fraction was in the supernatant. The supernatant was centrifuged at 13,000 rpm for 15 min. The nuclear pellet was washed three times in a lysis buffer. The nuclei were solubilized in buffer B [20 mM Hepes (pH 7.9), 400 mM

NaCl, 1 mM EDTA, 1 mM EGTA, 1 mM DTT, and 5% NP-40], incubated on ice for 20 min, and then centrifuged at 12,000 rpm for 10 min to remove insoluble components. All buffers used throughout the experiment contained protease cocktail inhibitors (Roche, USA) (*61*).

Microarray analysis
Total RNA was purified from sorted Lin⁻ MECs from 8-week-old *Frmd3*$^{-/-}$ female mice and WT littermate using the RNeasy Micro Kit (Qiagen). The quality of RNA was assessed with the Agilent Bioanalyzer 2100 (AgilentTechnologies) by using the Agilent RNA 6000 Nano Kit (Agilent Technologies) according to the manufacturer's protocol. Up to 120 ng of RNA was amplified with the standard Total Prep RNA amplification kit (Ambion), and complementary RNA (2 μg) was amplified, labeled, and purified by using GeneChip 3′ IVT PLUS Reagent Kit following the manufacturer's instructions to obtain biotin-labeled cRNA. Array hybridization and wash were performed using GeneChip Hybridization, Wash and Stain Kit in Hybridization Oven 645 and Fluidics Station 450 following the manufacturer's instructions. After washing, the chip slides were scanned by GeneChip Scanner 3000 and Command Console Software 4.0 with default settings. Raw data were normalized by the MAS 5.0 algorithm, affy packages in R. Subsequent analysis was carried out in R46 using the limma package 47. The differential genes are listed in table S5. Probes with false discovery rate <0.05 and fold change ≥2 were considered DE. The screened genes were compared with already reported basal MEC signatures [www.nature.com/articles/ncb3533#Sec34 www.cell.com/cell-stem-cell/fulltext/S1934-5909 (13)00148-3?_returnURL=https%3A%2F% 2Flinkinghub.elsevier.com%2Fretrieve%2Fpii%2FS1934590913001483%3Fshowall%3Dtrue#supplementaryMaterial; table S5] (*33*, *34*) and EMT/CSC-related gene signatures (www.nature.com/articles/ncb2607#Sec28; table S5) (*35*).

Bulk RNA sequencing
The total RNA was extracted using TRIzol reagent following the mRNA purification kit protocol (Invitrogen). The isolated mRNAs were fragmented into shorter fragments using a fragmentation buffer. Subsequently, double-stranded cDNA was synthesized using these short fragments as templates. The resulting cDNA underwent end-repair, ligation to Illumina adapters, size selection on an agarose gel [approximately 250 base pairs (bp)], and PCR amplification. Last, the cDNA library was sequenced on an Illumina NovaSeq 6000 sequencing platform. HISAT2 software was used to align the Fastqc document with the GRCh38 human reference genome, while Samtools and FeatureCounts were used for gene expression quantification. Bulk RNA-seq data of MCF-7 and T47D cells with *FRMD3* knockdown are available at the Gene Expression Omnibus (accession number GSE253455; www.ncbi.nlm.nih.gov/geo/).

Single-cell RNA sequencing
scRNA-seq libraries were prepared using the Chromium Single Cell 3′ Reagent Kits v3 (10x Genomics) according to the manufacturer's instructions. Briefly, approximately 1×10^5 cells per FACS-sorted cell were washed with 0.04% bovine serum albumin Dulbecco's PBS three times and were resuscitated to a concentration of 700 to 1200 cells/μl (viability, ≥85%). Cells were captured in droplets at a targeted cell recovery of cells. After the reverse transcription step, emulsions were broken and barcoded cDNA was purified with Dynabeads, followed by PCR amplification. Amplified cDNA was then used for

3′ gene expression library construction. For gene expression library construction, 50 ng of amplified cDNA was fragmented and end-repaired, double size–selected with SPRIselect beads, and sequenced on a NovaSeq platform (Illumina) to generate 150-bp paired-end reads (62). The raw scRNA-seq data are available under accession code GSE252083. Before analysis, cells were filtered with unique molecular identifier counts below 30,000 and gene counts between 200 and 5000, and then the cell content of more than 20% mitochondrial was removed. After filtering, the functions in Seurat v2.3 are used for dimensionality reduction and clustering. NormalizeData and ScaleData functions are used to normalize and scale all gene expression, and with the FindVariableFeatures function, the 2000 most notably changed genes were selected for principal components analysis. The genes were divided into multiple groups with FindClusters, and the batch effect between samples was removed with the Harnomy package. The data were visualized in two-dimensional space with Uniform Manifold Approximation and Projection visualization.

Statistical analysis

Statistical analysis for comparing two experimental groups was performed using Student's t tests. Kaplan-Meier curves were used to analyze survival. A value of $P < 0.05$ was considered statistically significant. Analyses were performed with Prism 9.0 (GraphPad software). Differences are labeled ns for not significant, * for $P \leq 0.05$, ** for $P \leq 0.01$, *** for $P \leq 0.001$, and **** for $P \leq 0.0001$. Pre-established criteria for the removal of animals from the experiment were based on animal health, behavior, and well-being as required by ethical guidelines. The Wilcoxon-based nonparametric test method is used with Seurat FindMarkers function, and selected genes expressed in more than 10% of cells per one cluster, genes whose average log (fold change) > 0.5 were marked as DE genes.

Binding pattern analysis

We combined the resolved homologous domain of the protein with the AlphaFold to predict the structure of the entire protein, with the FRMD3 predicted structure set to blue and the Disheveled-2 predicted structure set to green. We uploaded the prediction results to the GRAMM website (https://gramm.compbio.ku.edu/request). Then, we conducted molecular docking simulation, analyzed the simulation results, and selected the docking mode that met our requirements.

Supplementary Materials

This PDF file includes:
Figs. S1 to S8
Tables S1 to S4
Legend for table S5

Other Supplementary Material for this manuscript includes the following:
Table S5

REFERENCE AND NOTES

1. G. Bianchini, J. M. Balko, I. A. Mayer, M. E. Sanders, L. Gianni, Triple-negative breast cancer: Challenges and opportunities of a heterogeneous disease. *Nat. Rev. Clin. Oncol.* **13**, 674–690 (2016).

2. P. Alluri, L. A. Newman, Basal-like and triple-negative breast cancers: Searching for positives among many negatives. *Surg. Oncol. Clin. N. Am.* **23**, 567–577 (2014).

3. S. Elsamany, S. Abdullah, Triple-negative breast cancer: Future prospects in diagnosis and management. *Med. Oncol.* **31**, 834 (2014).

4. L. Malorni, P. B. Shetty, C. de Angelis, S. Hilsenbeck, M. F. Rimawi, R. Elledge, C. K. Osborne, S. de Placido, G. Arpino, Clinical and biologic features of triple-negative breast cancers in a large cohort of patients with long-term follow-up. *Breast Cancer Res. Treat.* **136**, 795–804 (2012).

5. M. Zhang, A. V. Lee, J. M. Rosen, The cellular origin and evolution of breast cancer. *Cold Spring Harb. Perspect. Med.* **7**, (2017).

6. A. Skibinski, C. Kuperwasser, The origin of breast tumor heterogeneity. *Oncogene* **34**, 5309–5316 (2015).

7. T. Celia-Terrassa, Mammary stem cells and breast cancer stem cells: Molecular connections and clinical implications. *Biomedicine* **6**, 50 (2018).

8. A. Prat, C. M. Perou, Mammary development meets cancer genomics. *Nat. Med.* **15**, 842–844 (2009).

9. B. Tiede, Y. Kang, From milk to malignancy: The role of mammary stem cells in development, pregnancy and breast cancer. *Cell Res.* **21**, 245–257 (2011).

10. J. E. Visvader, Keeping abreast of the mammary epithelial hierarchy and breast tumorigenesis. *Genes Dev.* **23**, 2563–2577 (2009).

11. J. E. Visvader, J. Stingl, Mammary stem cells and the differentiation hierarchy: Current status and perspectives. *Genes Dev.* **28**, 1143–1158 (2014).

12. N. Takebe, P. J. Harris, R. Q. Warren, S. P. Ivy, Targeting cancer stem cells by inhibiting Wnt, Notch, and Hedgehog pathways. *Nat. Rev. Clin. Oncol.* **8**, 97–106 (2011).

13. P. M. Siegel, W. J. Muller, Transcription factor regulatory networks in mammary epithelial development and tumorigenesis. *Oncogene* **29**, 2753–2759 (2010).

14. M. L. Asselin-Labat, K. D. Sutherland, H. Barker, R. Thomas, M. Shackleton, N. C. Forrest, L. Hartley, L. Robb, F. G. Grosveld, J. van der Wees, G. J. Lindeman, J. E. Visvader, Gata-3 is an essential regulator of mammary-gland morphogenesis and luminal-cell differentiation. *Nat. Cell Biol.* **9**, 201–209 (2007).

15. F. Lopez-Moncada, E. A. Castellon, H. R. Contreras, The transcription factors Zeb1 and snail induce cell malignancy and cancer stem cell phenotype in prostate cells, increasing androgen synthesis capacity and therapy resistance. *Adv. Exp. Med. Biol.* **1393**, 51–64 (2022).

16. A. M. Lilja, V. Rodilla, M. Huyghe, E. Hannezo, C. Landragin, O. Renaud, O. Leroy, S. Rulands, B. D. Simons, S. Fre, Clonal analysis of Notch1-expressing cells reveals the existence of unipotent stem cells that retain long-term plasticity in the embryonic mammary gland. *Nat. Cell Biol.* **20**, 677–687 (2018).

17. Z. Wang, L. Zhang, B. Li, J. Song, M. Yu, J. Zhang, C. Chen, J. Zhan, H. Zhang, Kindlin-2 in myoepithelium controls luminal progenitor commitment to alveoli in mouse mammary gland. *Cell Death Dis.* **14**, 675 (2023).

18. T. Bouras, B. Pal, F. Vaillant, G. Harburg, M. L. Asselin-Labat, S. R. Oakes, G. J. Lindeman, J. E. Visvader, Notch signaling regulates mammary stem cell function and luminal cell-fate commitment. *Cell Stem Cell* **3**, 429–441 (2008).

19. S. J. Chatterjee, R. Halaoui, R. C. Deagle, C. Rejon, L. McCaffrey, Numb regulates cell tension required for mammary duct elongation. *Biol. Open* **8**, bio042341 (2019).

20. C. Yi, J. L. Kissil, Merlin in organ size control and tumorigenesis: Hippo versus EGFR? *Genes Dev.* **24**, 1673–1679 (2010).

21. J. Larsson, M. Ohishi, B. Garrison, M. Aspling, V. Janzen, G. B. Adams, M. Curto, A. I. McClatchey, E. Schipani, D. T. Scadden, Nf2/merlin regulates hematopoietic stem cell behavior by altering microenvironmental architecture. *Cell Stem Cell* **3**, 221–227 (2008).

22. D. Haase, M. Meister, T. Muley, J. Hess, S. Teurich, P. Schnabel, B. Hartenstein, P. Angel, FRMD3, a novel putative tumour suppressor in NSCLC. *Oncogene* **26**, 4464–4468 (2007).

23. C. Curtis, S. P. Shah, S.-F. Chin, G. Turashvili, O. M. Rueda, M. J. Dunning, D. Speed, A. G. Lynch, S. Samarajiwa, Y. Yuan, S. Gräf, G. Ha, G. Haffari, A. Bashashati, R. Russell, S. M. Kinney; METABRIC Group, A. Langerød, A. Green, E. Provenzano, G. Wishart, S. Pinder, P. Watson, F. Markowetz, L. Murphy, I. Ellis, A. Purushotham, A.-L. Børresen-Dale, J. D. Brenton, S. Tavaré, C. Caldas, S. Aparicio, The genomic and transcriptomic architecture of 2,000 breast tumours reveals novel subgroups. *Nature* **486**, 346–352 (2012).

24. J. I. Herschkowitz, K. Simin, V. J. Weigman, I. Mikaelian, J. Usary, Z. Hu, K. E. Rasmussen, L. P. Jones, S. Assefnia, S. Chandrasekharan, M. G. Backlund, Y. Yin, A. I. Khramtsov, R. Bastein, J. Quackenbush, R. I. Glazer, P. H. Brown, J. E. Green, L. Kopelovich, P. A. Furth, J. P. Palazzo, O. I. Olopade, P. S. Bernard, G. A. Churchill, T. van Dyke, C. M. Perou, Identification of conserved gene expression features between murine mammary carcinoma models and human breast tumors. *Genome Biol.* **8**, R76 (2007).

25. B. D. Lehmann, J. A. Bauer, X. Chen, M. E. Sanders, A. B. Chakravarthy, Y. Shyr, J. A. Pietenpol, Identification of human triple-negative breast cancer subtypes and preclinical models for selection of targeted therapies. *J. Clin. Invest.* **121**, 2750–2767 (2011).

26. C. M. Perou, A. L. Borresen-Dale, Systems biology and genomics of breast cancer. *Cold Spring Harb. Perspect. Biol.* **3**, a003293 (2011).

27. E. Lim, F. Vaillant, D. Wu, N. C. Forrest, B. Pal, A. H. Hart, M.-L. Asselin-Labat, D. E. Gyorki, T. Ward, A. Partanen, F. Feleppa, L. I. Huschtscha, H. J. Thorne, kConFab, S. B. Fox, M. Yan, J. D. French, M. A. Brown, G. K. Smyth, J. E. Visvader, G. J. Lindeman, Aberrant luminal

progenitors as the candidate target population for basal tumor development in BRCA1 mutation carriers. *Nat. Med.* **15**, 907–913 (2009).

28. A. Nassar, Z. M. Sussman, D. Lawson, C. Cohen, Inference of the Basal epithelial phenotype in breast carcinoma from differential marker expression, using tissue microarrays in triple negative breast cancer and women younger than 35. *Breast J.* **18**, 399–405 (2012).

29. S. Zhang, W. C. Chung, G. Wu, S. E. Egan, L. Miele, K. Xu, Manic fringe promotes a claudin-low breast cancer phenotype through notch-mediated PIK3CG induction. *Cancer Res.* **75**, 1936–1943 (2015).

30. C. A. Livasy, G. Karaca, R. Nanda, M. S. Tretiakova, O. I. Olopade, D. T. Moore, C. M. Perou, Phenotypic evaluation of the basal-like subtype of invasive breast carcinoma. *Mod. Pathol.* **19**, 264–271 (2006).

31. A. Wang, S. Arantes, L. Yan, K. Kiguchi, M. J. McArthur, A. Sahin, H. D. Thames, C. M. Aldaz, M. C. MacLeod, The transcription factor ATF3 acts as an oncogene in mouse mammary tumorigenesis. *BMC Cancer* **8**, 268 (2008).

32. J. L. Inman, C. Robertson, J. D. Mott, M. J. Bissell, Mammary gland development: Cell fate specification, stem cells and the microenvironment. *Development* **142**, 1028–1042 (2015).

33. B. Gu, K. Watanabe, P. Sun, M. Fallahi, X. Dai, Chromatin effector Pygo2 mediates Wnt-notch crosstalk to suppress luminal/alveolar potential of mammary stem and basal cells. *Cell Stem Cell* **13**, 48–61 (2013).

34. T. Celià-Terrassa, D. D. Liu, A. Choudhury, X. Hang, Y. Wei, J. Zamalloa, R. Alfaro-Aco, R. Chakrabarti, Y.-Z. Jiang, B. I. Koh, H. A. Smith, C. De Coste, J.-J. Li, Z.-M. Shao, Y. Kang, Normal and cancerous mammary stem cells evade interferon-induced constraint through the miR-199a-LCOR axis. *Nat. Cell Biol.* **19**, 711–723 (2017).

35. R. Chakrabarti, J. Hwang, M. Andres Blanco, Y. Wei, M. Lukačišin, R. A. Romano, K. Smalley, S. Liu, Q. Yang, T. Ibrahim, L. Mercatali, D. Amadori, B. G. Haffty, S. Sinha, Y. Kang, Elf5 inhibits the epithelial-mesenchymal transition in mammary gland development and breast cancer metastasis by transcriptionally repressing Snail2. *Nat. Cell Biol.* **14**, 1212–1222 (2012).

36. M. Shackleton, F. Vaillant, K. J. Simpson, J. Stingl, G. K. Smyth, M. L. Asselin-Labat, L. Wu, G. J. Lindeman, J. E. Visvader, Generation of a functional mammary gland from a single stem cell. *Nature* **439**, 84–88 (2006).

37. J. C. Liu, T. Deng, R. S. Lehal, J. Kim, E. Zacksenhaus, Identification of tumorsphere- and tumor-initiating cells in HER2/Neu-induced mammary tumors. *Cancer Res.* **67**, 8671–8681 (2007).

38. C. Grange, S. Lanzardo, F. Cavallo, G. Camussi, B. Bussolati, Sca-1 identifies the tumor-initiating cells in mammary tumors of BALB-neuT transgenic mice. *Neoplasia* **10**, 1433–1443 (2008).

39. T. Doerks, R. R. Copley, J. Schultz, C. P. Ponting, P. Bork, Systematic identification of novel protein domain families associated with nuclear functions. *Genome Res.* **12**, 47–56 (2002).

40. Y. Hu, G. K. Smyth, ELDA: Extreme limiting dilution analysis for comparing depleted and enriched populations in stem cell and other assays. *J. Immunol. Methods* **347**, 70–78 (2009).

41. K. McCune, R. Mehta, M. A. Thorat, S. Badve, H. Nakshatri, Loss of ERα and FOXA1 expression in a progression model of luminal type breast cancer: Insights from PyMT transgenic mouse model. *Oncol. Rep.* **24**, 1233–1239 (2010).

42. S. Pece, D. Tosoni, S. Confalonieri, G. Mazzarol, M. Vecchi, S. Ronzoni, L. Bernard, G. Viale, P. G. Pelicci, P. P. di Fiore, Biological and molecular heterogeneity of breast cancers correlates with their cancer stem cell content. *Cell* **140**, 62–73 (2010).

43. C. L. Chaffer, N. D. Marjanovic, T. Lee, G. Bell, C. G. Kleer, F. Reinhardt, A. C. D'Alessio, R. A. Young, R. A. Weinberg, Poised chromatin at the ZEB1 promoter enables breast cancer cell plasticity and enhances tumorigenicity. *Cell* **154**, 61–74 (2013).

44. W. Guo, Z. Keckesova, J. L. Donaher, T. Shibue, V. Tischler, F. Reinhardt, S. Itzkovitz, A. Noske, U. Zürrer-Härdi, G. Bell, W. L. Tam, S. A. Mani, A. van Oudenaarden, R. A. Weinberg, Slug and Sox9 cooperatively determine the mammary stem cell state. *Cell* **148**, 1015–1028 (2012).

45. A. P. Morel, C. Ginestier, R. M. Pommier, O. Cabaud, E. Ruiz, J. Wicinski, M. Devouassoux-Shisheboran, V. Combaret, P. Finetti, C. Chassot, C. Pinatel, F. Fauvet, P. Saintigny, E. Thomas, C. Moyret-Lalle, J. Lachuer, E. Despras, J. L. Jauffret, F. Bertucci, J. Guitton, A. Wierinckx, Q. Wang, N. Radosevic-Robin, F. Penault-Llorca, D. G. Cox, F. Hollande, S. Ansieau, J. Caramel, D. Birnbaum, A. M. Vigneron, A. Tissier, E. Charafe-Jauffret, A. Puisieux, A stemness-related ZEB1-MSRB3 axis governs cellular pliancy and breast cancer genome stability. *Nat. Med.* **23**, 568–578 (2017).

46. A. Raouf, Y. Zhao, K. To, J. Stingl, A. Delaney, M. Barbara, N. Iscove, S. Jones, S. McKinney, J. Emerman, S. Aparicio, M. Marra, C. Eaves, Transcriptome analysis of the normal human mammary cell commitment and differentiation process. *Cell Stem Cell* **3**, 109–118 (2008).

47. L. Melchor, G. Molyneux, A. Mackay, F. A. Magnay, A. Atienza, H. Kendrick, D. Nava-Rodrigues, M. Á. López-García, F. Milanezi, K. Greenow, D. Robertson, J. Palacios, J. S. Reis-Filho, M. J. Smalley, Identification of cellular and genetic drivers of breast cancer heterogeneity in genetically engineered mouse tumour models. *J. Pathol.* **233**, 124–137 (2014).

48. K. Xu, J. Usary, P. C. Kousis, A. Prat, D. Y. Wang, J. R. Adams, W. Wang, A. J. Loch, T. Deng, W. Zhao, R. D. Cardiff, K. Yoon, N. Gaiano, V. Ling, J. Beyene, E. Zacksenhaus, T. Gridley,

W. L. Leong, C. J. Guidos, C. M. Perou, S. E. Egan, Lunatic fringe deficiency cooperates with the Met/Caveolin gene amplicon to induce basal-like breast cancer. *Cancer Cell* **21**, 626–641 (2012).

49. R. Chakrabarti, Y. Wei, J. Hwang, X. Hang, M. A. Blanco, A. Choudhury, B. Tiede, R.-A. Romano, C. De Coste, L. Mercatali, T. Ibrahim, D. Amadori, N. Kannan, C. J. Eaves, S. Sinha, Y. Kang, DeltaNp63 promotes stem cell activity in mammary gland development and basal-like breast cancer by enhancing Fzd7 expression and Wnt signalling. *Nat. Cell Biol.* **16**, 1004–1015 (2014).

50. L. Tao, D. Xiang, Y. Xie, R. T. Bronson, Z. Li, Induced p53 loss in mouse luminal cells causes clonal expansion and development of mammary tumours. *Nat. Commun.* **8**, 14431 (2017).

51. S. Koren, L. Reavie, J. P. Couto, D. de Silva, M. B. Stadler, T. Roloff, A. Britschgi, T. Eichlisberger, H. Kohler, O. Aina, R. D. Cardiff, M. Bentires-Alj, PIK3CA(H1047R) induces multipotency and multi-lineage mammary tumours. *Nature* **525**, 114–118 (2015).

52. Y. A. Zeng, R. Nusse, Wnt proteins are self-renewal factors for mammary stem cells and promote their long-term expansion in culture. *Cell Stem Cell* **6**, 568–577 (2010).

53. B. T. MacDonald, K. Tamai, X. He, Wnt/beta-catenin signaling: Components, mechanisms, and diseases. *Dev. Cell* **17**, 9–26 (2009).

54. G. M. Collu, A. Hidalgo-Sastre, A. Acar, L. Bayston, C. Gildea, M. K. Leverentz, C. G. Mills, T. W. Owens, O. Meurette, K. Dorey, K. Brennan, Dishevelled limits Notch signalling through inhibition of CSL. *Development* **139**, 4405–4415 (2012).

55. L. Wang, A. N. Brooks, J. Fan, Y. Wan, R. Gambe, S. Li, S. Hergert, S. Yin, S. S. Freeman, J. Z. Levin, L. Fan, M. Seiler, S. Buonamici, P. G. Smith, K. F. Chau, C. L. Cibulskis, W. Zhang, L. Z. Rassenti, E. M. Ghia, T. J. Kipps, S. Fernandes, D. B. Bloch, D. Kotliar, D. A. Landau, S. A. Shukla, J. C. Aster, R. Reed, D. S. DeLuca, J. R. Brown, D. Neuberg, G. Getz, K. J. Livak, M. M. Meyerson, P. V. Kharchenko, C. J. Wu, Transcriptomic characterization of SF3B1 mutation reveals its pleiotropic effects in chronic lymphocytic leukemia. *Cancer Cell* **30**, 750–763 (2016).

56. S. P. Grogan, T. Olee, K. Hiraoka, M. K. Lotz, Repression of chondrogenesis through binding of notch signaling proteins HES-1 and HEY-1 to N-box domains in the COL2A1 enhancer site. *Arthritis Rheum.* **58**, 2754–2763 (2008).

57. T. J. Mead, K. E. Yutzey, Notch pathway regulation of chondrocyte differentiation and proliferation during appendicular and axial skeleton development. *Proc. Natl. Acad. Sci. U.S.A.* **106**, 14420–14425 (2009).

58. S. Sale, D. Lafkas, S. Artavanis-Tsakonas, Notch2 genetic fate mapping reveals two previously unrecognized mammary epithelial lineages. *Nat. Cell Biol.* **15**, 451–460 (2013).

59. B. Gu, P. Sun, Y. Yuan, R. C. Moraes, A. Li, A. Teng, A. Agrawal, C. Rhéaume, V. Bilanchone, J. M. Veltmaat, K. I. Takemaru, S. Millar, E. Y. H. P. Lee, M. T. Lewis, B. Li, X. Dai, Pygo2 expands mammary progenitor cells by facilitating histone H3 K4 methylation. *J. Cell Biol.* **185**, 811–826 (2009).

60. X. Man, Q. Li, B. Wang, H. Zhang, S. Zhang, Z. Li, DNMT3A and DNMT3B in breast tumorigenesis and potential therapy. *Front. Cell Dev. Biol.* **10**, 916725 (2022).

61. J. Song, T. Wang, W. Xu, P. Wang, J. Wan, Y. Wang, J. Zhan, H. Zhang, HOXB9 acetylation at K27 is responsible for its suppression of colon cancer progression. *Cancer Lett.* **426**, 63–72 (2018).

62. G. Q. Zhu, Z. Tang, R. Huang, W. F. Qu, Y. Fang, R. Yang, C. Y. Tao, J. Gao, X. L. Wu, H. X. Sun, Y. F. Zhou, S. S. Song, Z. B. Ding, Z. Dai, J. Zhou, D. Ye, D. J. Wu, W. R. Liu, J. Fan, Y. H. Shi, CD36⁺ cancer-associated fibroblasts provide immunosuppressive microenvironment for hepatocellular carcinoma via secretion of macrophage migration inhibitory factor. *Cell Discov.* **9**, 25 (2023).